ORNL/TM-2023/3024

Analysis of WIRE-21 SPND and Optical Fiber Sensor Measurements

Daniel C. Sweeney
Padhraic L. Mulligan
Christian M. Petrie

August 2023

OAK RIDGE National Laboratory

ORNL IS MANAGED BY UT-BATTELLE LLC FOR THE US DEPARTMENT OF ENERGY

ORNL/TM-2023/3024

NEET-ASI

Analysis of WIRE-21 SPND and Optical Fiber Sensor Measurements

Daniel C. Sweeney,
Padhraic L. Mulligan,
Christian M. Petrie

Milestones M3CT-23OR0702071 and M3CT-23OR0702064
August 2023

Prepared by
OAK RIDGE NATIONAL LABORATORY
Oak Ridge, TN 37831
managed by
UT-Battelle LLC
for the
US DEPARTMENT OF ENERGY
under contract DE-AC05-00OR22725

CONTENTS

LIST OF FIGURES

LIST OF TABLES

ABBREVIATIONS

BOC	beginning of cycle
EOC	end of cycle
FBG	fiber Bragg grating
EFPD	effective full-power day
FUT	fiber under test
HCF	hollow+core fiber
HFIR	High Flux Isotope Reactor
ILC	Idaho Laboratories Corporation
MI	mineral insulated
MITR	Massachusetts Institute of Technology Reactor
MOC	middle of cycle
OFDR	optical frequency-domain reflectometry
ORNL	Oak Ridge National Laboratory
OSURR	Ohio State University Research Reactor
PCC	Pearson Correlation Coefficient
RAL	random air-line (Fiber)
RB	removable beryllium
RBS	Rayleigh backscatter
SPND	Self-Powered Neutron Detector
UV	ultraviolet
WEC	Westinghouse Electric Company
WIRE-21	Wireless Instrumented RB Experiment 2021

ABSTRACT

The Wireless Instrumented RB Experiment 2021 (WIRE-21) was a highly instrumented experiment designed to test prototype wireless temperature and pressure sensors developed by Westinghouse Electric Corporation (WEC) in the High Flux Isotope Reactor (HFIR). In addition to these sensors, a suite of other sensors was also integrated into the experiment capsule, including various types of distributed optical fiber sensors and self-powered neutron detectors (SPNDs). This report presents an analysis of the data generated by the SPNDs and optical fiber sensors that were tested under the highest reported neutron flux. The distributed optical fiber sensor results demonstrate that F-doped optical fibers, particularly those inscribed with fs fiber Bragg gratings (FBGs), are capable of surviving fast neutron fluences on the order of 10^{21} n_{fast}/cm^2 at temperatures relevant to light-water reactors (between 200 and 400°C). However, a significant blue-shift in the optical spectra of these sensors was observed over the course of irradiation which cannot be explained based on the current understanding of radiation-induced compaction in fused silica glass. A mechanistic understanding of this drift has not yet been developed and is proposed as future scope under the Advanced Sensors and Instrumentation program. Of the four SPNDs, only one appeared to operate normally during three cycles of irradiation. A radiation transport model of the experiment in HFIR was used to determine time-dependent neutron flux in this SPND and to calculate the neutron sensitivity of the device. Results showed a cycle averaged sensitivity of 1.5×10^{-22} and 1.4×10^{-22} $A/n\nu$ for the first and third cycles of irradiation, respectively. Additional details pertaining to the optical fibers and SPNDs are included herein.

1. INTRODUCTION

The Wireless Instrumented RB Experiment 2021 (WIRE-21) was a highly instrumented experiment designed to test prototype wireless sensors developed by Westinghouse Electric Corporation (WEC) in the High Flux Isotope Reactor (HFIR) [1]. The wireless sensors were designed to measure temperatures similar to those expected at the centerline of light-water reactor fuel pellets, and they were also designed to measure light-water reactor fuel rod internal pressures [2, 3]. More specific details regarding the WEC temperature and pressure sensors and early results from this experiment are detailed in the literature [4, 5, 6]. In addition to the work performed using the WEC sensors, the experiment included a multitude of active and passive instrumentation to measure local and distributed temperatures, as well as the neutron flux, flux energy spectrum, and fluence over several HFIR cycles. The WIRE-21 experiment was irradiated for 75.9 effective full power days (EFPDs) to maximum thermal and fast neutron fluences of 5.8×10^{21} n_{th}/cm^2 and 3.4×10^{21} n_{fast}/cm^2, respectively, at temperatures between 200 and 400 °C. The WIRE-21 experiment was the most highly instrumented experiment performed in HFIR over its 58-year operational history, and the infrastructure established to support it will enable future irradiation testing and in-situ monitoring of advanced optical and electronic sensors.

This report presents data recorded from 8 distributed optical fiber sensors and 4 self-powered neutron detectors (SPNDs) that were irradiated as part of the WIRE-21 experiment. Most of the optical fiber sensors were commercially available Ge- or F-doped singlemode fused silica optical fibers with or without inscribed fiber Bragg gratings (FBGs). The FBGs included conventional draw tower or ultraviolet (UV) gratings—designated as Type I—or FBGs inscribed using a femtosecond laser—designated as Type II. Two hollow-core fibers (HCFs) were also included in the experiment assembly. The SPNDs included in the WIRE-21 experiment were identically fabricated and positioned at various elevations in the experiment capsule at -15, -5, 5, and 15 cm relative to the vertical midplane of the core. Variations were included in the

radial distribution of the sensors to accommodate electrical and optical leads from other sensors.

HFIR is a beryllium-reflected, light-water–cooled and –moderated flux-trap type reactor that operates at 85 MW during cycles that last approximately 23—25 d each. The fuel region is surrounded by a concentric 0.3 m thick beryllium reflector which is divided into three sections: the removable reflector, the semipermanent reflector, and the permanent reflector (Figure 1). Several experimental facilities are incorporated into the removable beryllium (RB* positions) where instrumented experiments can be irradiated. WIRE-21 was irradiated in an RB* experimental facility (RB-5A) with thermal and fast neutron fluxes of approximately 1×10^{15} $n_{th}/cm^2/s$ and 0.5×10^{15} $n_{fast}/cm^2/s$, respectively. WIRE-21 was irradiated over 5 full or partial irradiation cycles in HFIR: Cycle 1A (498A), Cycle 1B (498B), Cycle 2 (499), Cycle 3A (500A), and Cycle 3B (500B). An experimental timeline is shown in Figure 2. The WIRE-21 experiment represents one of the few cases of optical fiber sensors being irradiated to such high fluences, and to the authors' knowledge, the experiment the first time that either optical fiber sensors or SPNDs have been used in HFIR. These data are critical to the development of advanced sensors for nuclear reactor applications, including both advanced reactors and in-situ monitoring during irradiations in test reactors to support nuclear fuels and materials qualification.

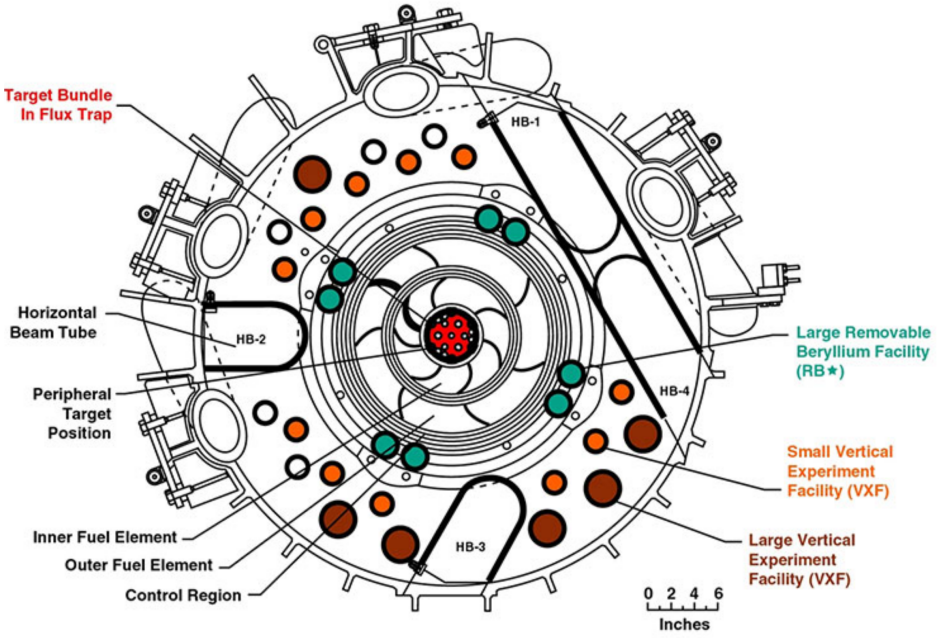

Figure 1. HFIR core layout.

2. OPTICAL FIBER SENSORS

The silica-based singlemode optical fibers were monitored during neutron irradiation using a combination of a commercially available optical frequency domain reflectometry (OFDR) interrogator (OBR-4600; Luna Innovations, Inc., Blacksburg, VA) and an optical multiplexer (FOS-008, Luna Innovations, Inc.). Multiple optical fibers were monitored as summarized in Table 1. This table describes the fibers that were tested, their OBR channels, and the lead fibers to which each fiber was joined to pass signals to/from the

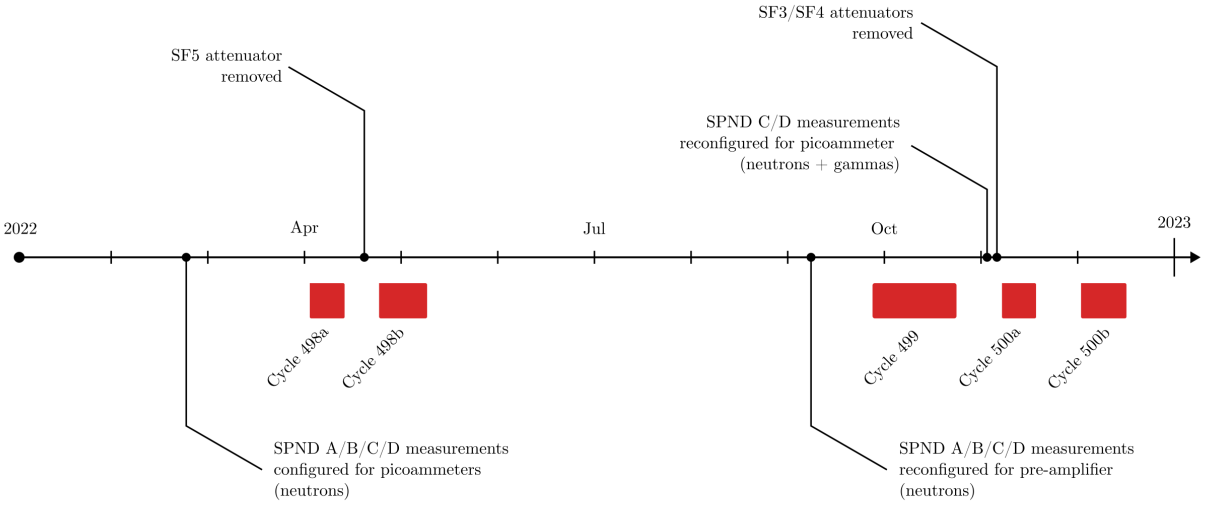

Figure 2. WIRE-21 experiment schedule.

Materials Irradiation Facility (MIF) where the OBR and optical multiplexer were located. Because a constant detector gain was used for all channels, attenuators had to be included for some channels with highly reflective FBGs to avoid saturating the detectors. The backscattered interference patterns were acquired approximately once every 5 minutes during irradiation in HFIR cycles 498, 499 and 500. Irradiation in HFIR was performed for 75.9 EFPDs to a maximum thermal (< 1 eV) neutron fluence, at the core centerline, of 6.0×10^{21} n_{th}/cm^2 (8.8×10^{15} $n_{th}/cm^2/s$) and 60 GGy (33 MGy/h). The fast (> 0.1 MeV) neutron fluence was calculated to be on the order of 3.0×10^{21} n_{fast}/cm^2 (4.5×10^{14} $n_{fast}/cm^2/s$). The FUTs were irradiated at temperatures in the 150–400 °C range.

2.1 ANALYTICAL METHODS

2.1.1 Optical Frequency-Domain Reflectometry

OFDR systems use a tunable laser to launch light into a fiber under test (FUT) over a narrow band of optical frequencies. At each of these frequencies ν, the intensity of the backscattered light is measured by an optical network that allows the light reflected along the FUT to interfere with light traveling through a reference fiber to generate an interference pattern based on the backscattered light profile [7, 8]. Figure 3 summarizes the backscattering process and the typical optical network for an OFDR system. Typically, a scan performed at time t comprises each polarization state ($S(\nu)$ and $P(\nu)$) measured by two separate photodetectors. These data are transformed into the spatial domain (x-domain) as a position along the axial length of the fiber using a Fourier transform

$$\langle S(t,x), P(t,x)\rangle = \mathcal{F}\Big\{\langle S(t,\nu), P(t,\nu)\rangle\Big\}, \tag{1}$$

where $S(x)$ and $P(x)$ are the reflected intensities of each polarization at each spatial position x and $\mathcal{F}\{\cdot\}$ indicates the Fourier transform. For quasi-distributed sensing applications, the FUT is then subdivided into

Table 1. Specifications for WIRE-21 fiber optic sensors. Note that the attenuators on SF3 and SF4 were removed after HFIR Cycle 499 and the attenuator on SF5 was removed after HFIR 498a.

ID	Channel	MIF Fiber	Fiber	Assembly	Attenuator
SF1	1	C	Pure SiO_2 core, F-doped cladding (SM1250SC(9/125)P, Fibercore)	SMF-28e+ Lead + 16 ft 12SM1250SC(9/125)P + 4 in termination	None
SF2	2	A	Ge-doped SiO_2 core, pure SiO_2 cladding (SMF-28e+, Corning)	SMF-28e+ Lead + 12 ft SM1250SC(9/125)P + 4 ft SMF-28e+ + 4 in termination	None
SF3	3	G	F-doped SiO_2 core and cladding (SM1250SC(9/125)P, Fibercore) + 9 fs gratings (FemtoFiberTec)	SMF-28e+ Lead + 12 ft SM1250SC(9/125)P + 28 in grating fiber + 4 in termination	FA05T-APC-1 (ThorLabs) 5.3 dB att./61.6 dB ref. (1310 nm) 5.32 dB att./61.2 dB ref. (1550 nm) **Removed after HFIR Cycle 499*
SF4	4	H	F-doped SiO_2 core and cladding (SM1250SC(9/125)P, Fibercore) + 6 fs gratings (FemtoFiberTec)	SMF-28e+ Lead + 12 ft SM1250SC(9/125)P + 28 in grating fiber + 4 in termination	FA05T-APC-1 (ThorLabs) 5.3 dB att./61.6 dB ref. (1310 nm) 5.44 dB att./61.1 dB ref. (1550 nm) **Removed after HFIR Cycle 499*
SF5	5	L	Pure SiO_2 core, F-doped cladding (SM1250SC(9/125)P, Fibercore) + 28 fs gratings (FemtoFiberTec)	SMF-28e+ Lead + 12 ft SM1250SC(9/125)P + 12 in grating fiber + 4 in termination	FA10T-APC-1 (ThorLabs) 10.6 dB att./61.5 dB ref. (1310 nm) 10.64 dB att./61.2 dB ref. (1550 nm) ***Removed after HFIR Cycle 498a*
SF6	6	J	Low bend loss fiber with UV gratings (AGF-A3A4-000, FBGS)	SMF-28e+ Lead + 12 ft SM1250SC(9/125)P + 4 ft grating fiber + 4 in termination	None
SF7	7	D	Hollow core PCF (HC-155, NKT Photonics)	SMF-28e+ Lead + 12 ft SM1250SC(9/125)P + 2.5 ft hollow core fiber + 15 cm SMF1250SC-(9/125)P	FA03T-APC-1 (ThorLabs) 2.75 dB att./61.5 dB ref. (1310 nm) 2.8 dB att./61.7 dB ref. (1550 nm)
SF8	8	M	Hollow core PCF (HC-155, NKT Photonics)	SMF-28e+ Lead + 12 ft SM1250SC(9/125)P + 2.5 ft hollow core fiber + 15 cm SMF1250SC-(9/125)P	FA03T-APC-1 (ThorLabs) 3.36 dB att./61.7 dB ref. (1310 nm) 3.4 dB att./61.2 dB ref. (1550 nm)

k subsections, and the magnitude of the optical intensity, $I_k(\nu)$, of subsection k is calculated as

$$I_k(t,\nu) = \mathcal{F}^{-1}\left\{\left\|\langle S(t,x), P(t,x)\rangle\right\|\right\}, \tag{2}$$

where $\mathcal{F}^{-1}\{\cdot\}$ is the inverse Fourier transform and $I_k(t,\nu)$ can be further normalized to

$$\bar{I}_k(t,\nu) = \frac{I_k(t,\nu) - \mu_k(t)}{\sigma_k(t)}, \tag{3}$$

where $\mu_k(t)$ and $\sigma_k(t)$ are the ν-domain average intensity and the standard deviation of $I_k(t,\nu)$. The decision to define $\mu_k(t)$ as the average intensity over the sensor k is heuristic, but could vary over subsection k or a subset of k and calculated using a running average, median, or other metric.

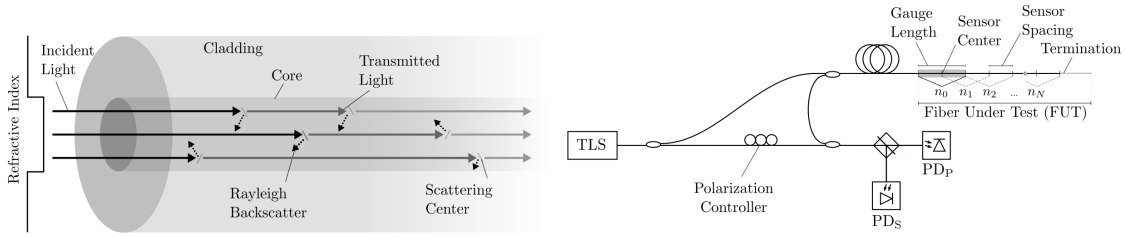

(a) Diagram of an optical fiber sensor **(b) Optical network in an OFDR instrument**

Figure 3. Schematic of optical fiber sensors interrogated using optical frequency-domain reflectometry (OFDR). Figure reprinted with permission from [8].

Temperature changes or mechanical strains experienced at subsection k will introduce a shift in the scan's measured optical spectrum and enable a combination of these parameters to be measured. Under the assumption that the RBS profile is stable in time and shifted only because of thermomechanical strain or thermo-optic effects, the spectral shift between an active scan of interest at time a, relative to a reference scan acquired at time r, can be calculated from the cross-correlation spectrum $C_k(a,r)$ as

$$C_k(a,r) = \bar{I}_k(a,\nu) \otimes \bar{I}_k(r,\nu). \tag{4}$$

The Pearson correlation coefficient (PCC) $\rho_k(a,r)$ and spectral shift $\Delta\nu_k(a,r)$ can then be calculated from $C_k(a,r)$ as

$$\rho_k(a,r) = \max\{C_k(a,r)\}, \tag{5}$$

and

$$\Delta\nu_k(a,r) = \operatorname{argmax}\{C_k(a,r)\}. \tag{6}$$

The measured spectral shift $\Delta\nu_k(a,r)$ can be related to changes in temperature and strain as

$$-\Delta\nu_k(a,r) = K_T\Delta T + K_\varepsilon\epsilon, \tag{7}$$

where K_T and K_ε are coefficients and ΔT and ε are the change in temperature and mechanical strain between scans a and r, respectively.

2.1.2 Graph Signal Processing for OFDR

Adaptive, graph methodologies are particularly well suited to resolving spectral shifts from distributed optical fiber sensors in nuclear environments, and they have been shown to account for the dynamicity of the Rayleigh backscatter (RBS) in these extreme conditions. The previous successes of these methods suggest that such graph-based approaches could be helpful in continuously resolving spectral shifts in the data acquired from the WIRE-21 optical fiber sensors. The graphical signal processing techniques described herein rely on the abstraction of the correlational measurements to a graphical network in which each node represents the RBS profile of an optical fiber at a specific time. In this framework, the edges connecting each pair of nodes represent the cross-correlation coefficient between the RBS at each node, and the correlational measurements are cast as a graph/network traversal problem (Figure 4). This approach is described in greater detail in previous work [9, 8, 10], where it was demonstrated to provide an optimal reconstruction; it was also shown that it can be implemented to take advantage of parallel processes. As such, the graph abstraction is only briefly reviewed here.

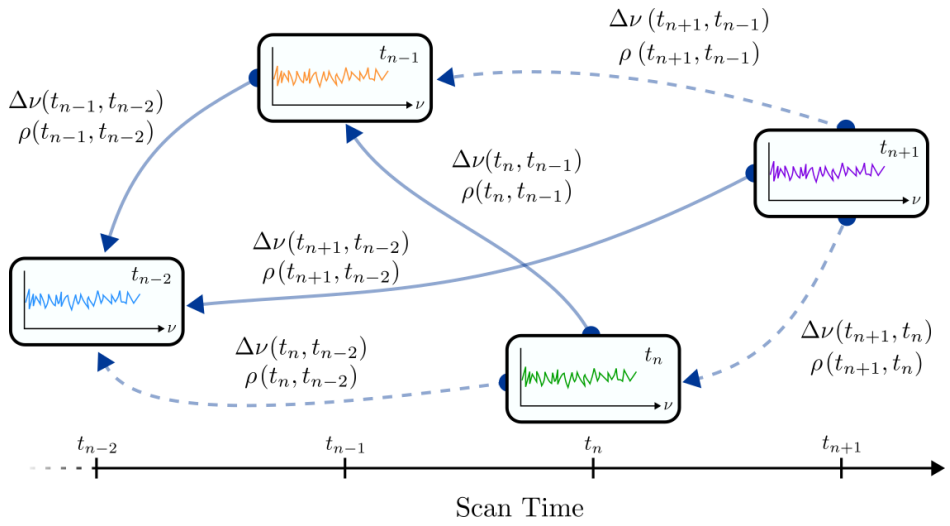

Figure 4. Schematic representation of graph created through comparisons of OFDR scans for one position axial position on an optical fiber sensors at different times.

An undirected graph $G_k = (T, \mathbf{A}_k)$ can be formed by considering the time series measurements for sensor k at times T as the nodes and a metric $M_k(t_{n-1}, t_n)$ as the weights of the edges connecting the nodes. The term $\mathbf{A}_k$ is the adjacency matrix defined as

$$\mathbf{A}_k = \begin{bmatrix} 0 & M_k(t_1, t_0) & \dots & M_k(t_{T-1}, t_0) & M_k(t_T, t_0) \\ 0 & 0 & \dots & M_k(t_{T-1}, t_1) & M_k(t_T, t_1) \\ \vdots & \vdots & \ddots & \vdots & \vdots \\ 0 & 0 & \dots & 0 & M_k(t_T, t_{T-1}) \\ 0 & 0 & \dots & 0 & 0 \end{bmatrix}, \tag{8}$$

with non-zero terms above the main diagonal. It should be noted that G_k is functionally considered directed under considerations of causality, meaning the target scan index must be larger than the index of the reference scan. Kruskal's algorithm [11] optimizes connections between all nodes and enables all cumulative measurements made on G_k to be eventually referenced back to the first scan acquired at t_0. The

metric $M_k(t_{n-1}, t_n)$ was implemented as the Pearson correlation coefficient (PCC)

$$M_k(t_{n-1}, t_n) = \rho_k(t_{n-1}, t_n). \tag{9}$$

In principle, the edge weight metric can be developed using one or a combination of several measures, in

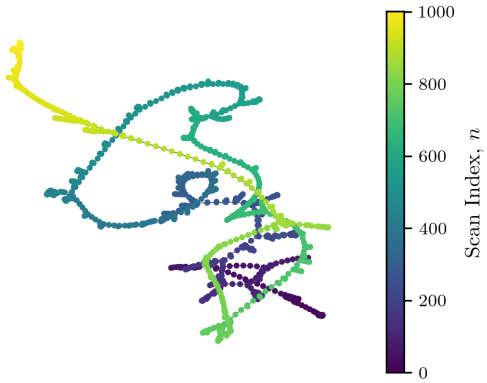

Figure 5. Example of a rooted graphical spanning tree of $G_k = (T, \mathbf{A}_k)$ derived from data from a sensing region (sensor) on optical fiber SF1 in WIRE-21.

addition to the PCC. For example, $M_k(t_{n-1}, t_n)$ could be defined the sum of square residuals (l^2-norm) between scans t_{n-1} and t_n as

$$M_k(t_{n-1}, t_n) = \left\| \bar{I}_k(t_n, \nu) - \bar{I}_k(t_{n-1}, \nu) \right\|_2, \tag{10}$$

where $\| \cdot \|_2$ indicates the l^2-norm taken when $\rho_k(t_n, t_{n-1})$ is maximized. This metric penalizes differences in spectral power and has been proposed, in combination with the PCC, to yield the composite metric $\bar{M}_k(t_{n-1}, t_n)$ [12], defined as

$$\bar{M}_k(t_{n-1}, t_n) = \rho_k(t_{n-1}, t_n) - \left\| \bar{I}_k(t_n, \nu) - \bar{I}_k(t_{n-1}, \nu) \right\|_2. \tag{11}$$

For the present work, $M_k(t_{n-1}, t_n) = \rho_k(t_{n-1}, t_n)$.

2.1.3 Graph-Tree Refactoring

This graphical analysis was performed after first sparsifying the graph, G_k, to compare only scan t_n with a maximum of 15 immediately preceding scans (in the range of $[t_{n-15}, t_{n-1}]$), which limited the computation time required for the analysis (i.e., efficiency of $O(n)$). A maximum spanning tree (MST) rooted to scan t_0 was calculated over G_k, then a cumulative summation was performed over the MST to recover the cumulative spectral shifts for each scan and spatial subdivision k. Two additional reprocessing steps were also investigated: (1) a refactoring routine in which jumps in spectral shift above a certain threshold are identified and iteratively replaced with the edge in G_k which minimized the change in spectral shift, and (2) a filtering approach on the spectral shift reconstruction. The median filter was implemented by first calculating the gradient in the spatial dimension (x), followed by using a two-dimensional median filter over the the five nearest spatial measurements ($[x_{k-2}, x_{k-1}, x_k, x_{k+1}, x_{k+2}]$) and three nearest temporal measurements ($[t_{n-1}, t_n, t_{n+1}]$). A cumulative sum over this filtered gradient was then performed to recover a filtered version of the original spectral shift signal.

2.2 RAYLEIGH BACKSCATTER SENSORS

2.2.1 Optical Intensity during Irradiation

Of the solid core optical fiber sensors installed in the WIRE-21 experiment (Table 1), two were installed without the the introduction of reflection-enhancing features such as FBGs: SF1, comprising a pure SiO_2 core and F-doped SiO_2 cladding, and SF2, comprising a Ge-doped SiO_2 core and pure SiO_2 cladding (Figure 6). Both of these fibers were terminated using coreless termination fiber and extended through the full length of the experiment. Though they were exposed to comparable conditions, their irradiation responses varied dramatically.

During cycle 498 (BOC 1), the RBS profile of SF1 showed changes in the shape and amplitude of reflections that occurred near the splice between the fiber waveguide and the coreless termination fiber (-10 cm) and at the end of the termination fiber (-20 cm). However, the intensities farther from these splices (-10 to 60 cm) were much less affected. Increased backscatter was observed closer to 20 cm above the core and that peak shifted upwards with increased irradiation time. This peak was attributed to Fresnel reflections that result from the spatially varying refractive index caused by spatial variations in radiation-induced compaction [13]. Closer to the center of the core these variations are less significant because the compaction process reaches an equilibrium at a high enough fast neutron fluence. Unfortunately SF1 was broken after the end of cycle 1 at a location outside of the reactor core during troubleshooting operations near the fiber leads. Hence, the data for this fiber from EOC 2 and EOC 3 are not useful. The backscattered intensities from SF2 dropped 15 dB within days of irradiation in HFIR (BOC 1, Figure 6b). Near the core centerline (0 cm) the intensities are indistinguishable from the noise floor of the system but some backscattered light could be measured farther above the core. For example, at 1.8 EFPDs, the intensity only decreased 5 dB relative to the pre-irradiation scan at a location 20 cm above the core centerline, whereas a 10 dB drop was observed 10 cm above the core centerline.

To compare the intensity (or amplitude) changes between SF1 and SF2 more directly, their intensities at positions 0 cm and 10 cm above the HFIR core centerline were compared over the course of the first irradiation cycle (HFIR cycle 498) [13]. These data show that the RBS amplitude of SF1 (denoted as F-RBS in Figure 7) initially experiences a slight increase with increasing fast neutron fluence, and then it decreases and approaches an apparent equilibrium value that is slightly higher than the backscattered amplitude of the pristine fiber. A similar equilibrium amplitude is reached for this fiber at the core centerline (0 cm) and at 10 cm. The RBS intensity of SF5, a pure SiO_2 core fiber with F-doped SiO_2 cladding inscribed with Type II FBGs, showed much larger decreases in backscattered intensity, eventually reaching an equilibrium intensity similar to SF1. These data suggest that the intensity of this equilibrium is stable and is a property of pure SiO_2 core/F-doped SiO_2 cladding optical fibers. As mentioned earlier, the initial increase in the amplitudes of SF1 are thought to be caused by Fresnel reflections that result from spatial variations in radiation-induced compaction and the associated increases in refractive index.

SF2 initially experiences a similar flux-dependent increase in amplitude caused by compaction-induced Fresnel reflections. However, the intensities then decrease by > 25 dB and eventually reach the measurement noise floor at fluences $< 1 \times 10^{20}$ n_{fast}/cm^2. These decreases in intensity were attributed to radiation-induced attenuation [13], which is known to be more significant in Ge-doped fibers [14].

2.2.2 Radiation-Induced Spectral Drift of Rayleigh Backscatter

In the WIRE-21 experiment, all included optical fibers were singlemode and were fabricated in SiO_2. Silica is an amorphous solid, and the RBS profile depends on the distribution of random density fluctuations that are created in the fiber during fabrication. However, irradiation damage alters the intensity and distribution of these fluctuations as local defect centers are generated. Because of this phenomenon, the RBS profile is not static, as it would be in non-nuclear environments. Additionally, the neutron damage has been shown to cause silica to compact, with the compaction depending on both temperature and fast neutron fluence, which is expected to cause a net blue-shift in the RBS spectrum [15]. Although these phenomena were anticipated at the outset of the experiment, they do not explain the magnitudes of the large blue-shifts observed during irradiation in WIRE-21 [13].

Figure 8 summarizes the measured spectral shifts for SF1 at various locations in comparison with shifts

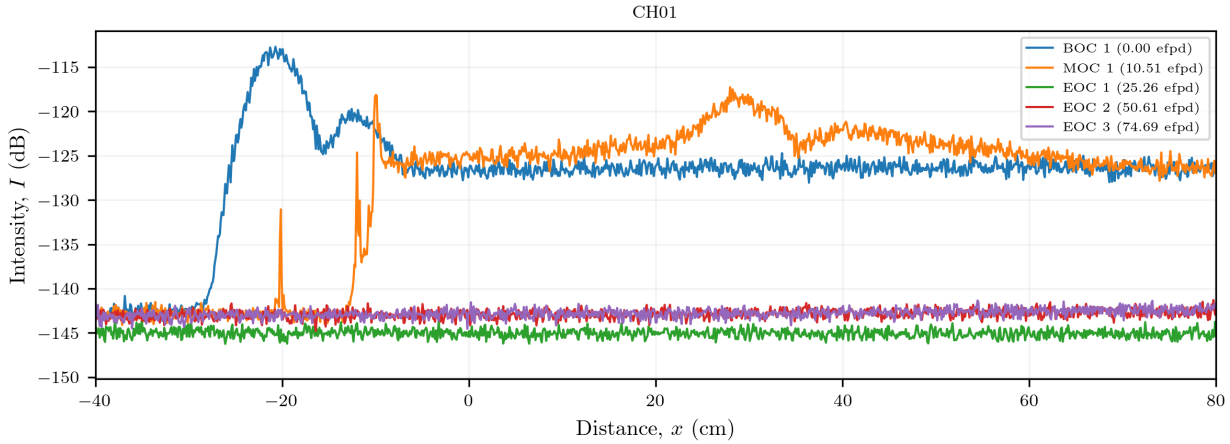

(a) SF1 Intensity

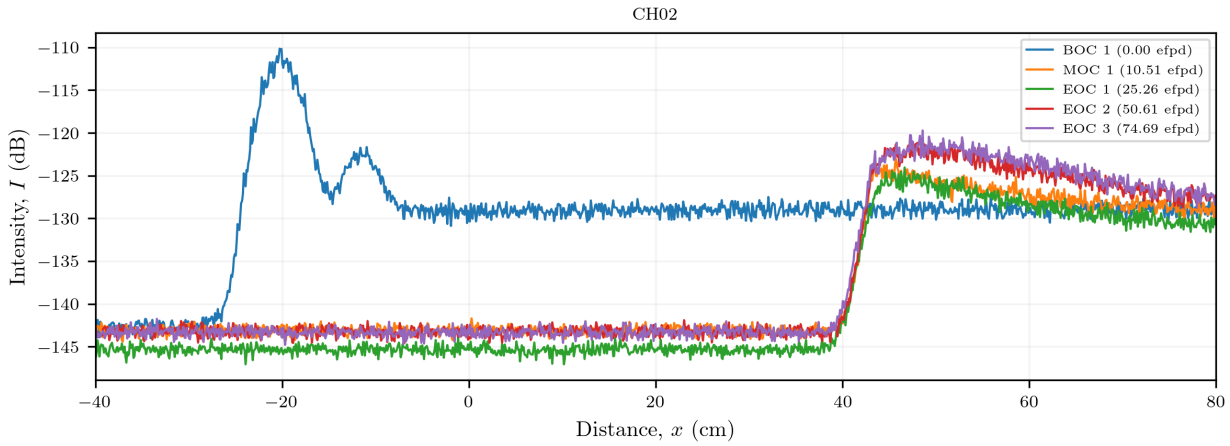

(b) SF2 Intensity

Figure 6. Non-grated optical fibers irradiated during WIRE-21. SF1 was a singlemode fiber with a pure SiO_2 core and F-doped SiO_2 cladding (a). SF2 was a singlemode fiber with a Ge-doped SiO_2 core with a pure SiO_2 cladding (b).

expected because of changes in temperature and radiation-induced compaction in SiO_2. The drift observed during irradiation was generally consistent with the shifts that were expected due to the combination of thermal effects and SiO_2 compaction for fast neutron fluences $< 1 \times 10^{20}$ n_{fast}/cm^2, although there were more significant inconsistencies at locations further from the core (18 and 30 cm above centerline). For fluences $> 1 \times 10^{20}$ n_{fast}/cm^2, the RBS spectrum exhibited unexpected blue shifts as large as 10 nm or greater over the first irradiation cycle. After the first irradiation cycle (HFIR cycle 498), the region of SF1 located 10 cm above the core had drifted the most, with a spectral shift of -11 nm, with lower positions drifting 8 to 10 nm (Figure 8a–d). The measured drifts were lower at locations farther from the core ($\geq$ 18 cm, Figure 8e–f). The mechanism responsible for the unexpected drift remains unclear and will be the focus of future analyses.

To characterize the drift rate, the slopes of the spectral shift $\Delta\nu$ at positions along SF1 were calculated for fluences $> 1 \times 10^{20}$ n_{fast}/cm^2 (Figure 9a). These data were able to be tracked using the graph analysis techniques discussed in Section 2.1.2, although it should be noted that the RBS profiles of SF1 close to the core (-5 to 5 cm) could not be tracked continuously beyond 20 d, and they did not change when the reactor was not in operation for 12 to 17 d. The negative slope of these curves, $-d(\Delta\lambda)/d\phi$, was calculated by fitting a linear function to the slope of these curves at fluences $> 1 \times 10^{20}$ n_{fast}/cm^2 (Figure 9b). The drift rate is somewhat similar to the axial fast neutron flux profile of the HFIR core, but the drift rate profile is slightly biased above the core centerline (at 5 cm). This trend suggests that the drift rate likely has a strong dependence on fast neutron flux and fluence, but there could be other dependencies on parameters such as temperature, which was measured to be highest closer to 5 cm. Interestingly, the spectral shift drift $\Delta\lambda$ does not appear to saturate during a single irradiation cycle ($> 1 \times 10^{20}$ n_{fast}/cm^2) which is contrary to a model that was developed previously based on measured radiation-induced compaction in bulk SiO_2 specimens [15]. These previous data suggest that radiation-induced compaction gives rise to up to a 2.0 to 2.5% volumetric compaction (0.07% Bragg wavelength shift), depending on the temperature and fast neutron fluence. The compaction becomes significant between 1×10^{18} to 1×10^{19} n_{fast}/cm^2 and saturates at fast neutron fluences between 1×10^{19} to 1×10^{20} n_{fast}/cm^2. The spectral shift of SF1 is well explained by a

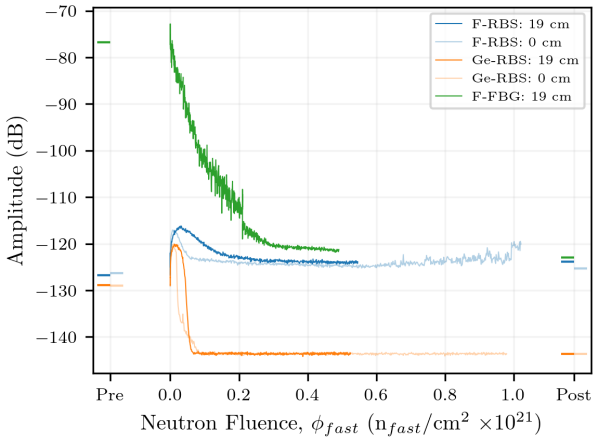

Figure 7. The Rayleigh backscatter intensity of irradiated fibers SF1 (F-RBS), SF2 (Ge-RBS), and SF5 (F-FBG) as a function of fast neutron fluence at various locations relative to the HFIR core midplane.

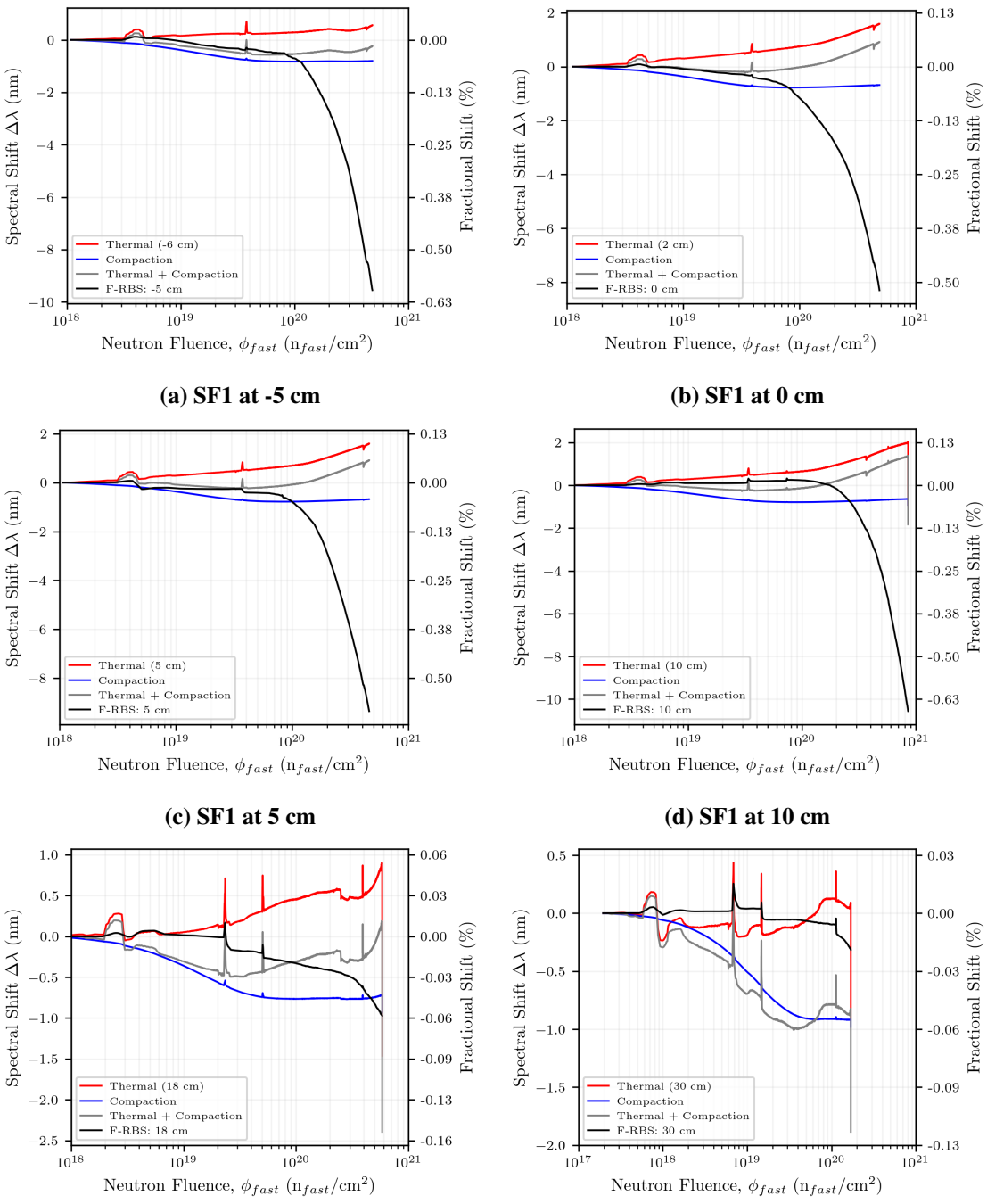

(a) SF1 at -5 cm

(b) SF1 at 0 cm

(c) SF1 at 5 cm

(d) SF1 at 10 cm

(e) SF1 at 18 cm

(f) SF1 at 30 cm

Figure 8. Shift of the Rayleigh backscatter spectrum from SF1 at positions along the fiber, relative to the HFIR center centerline. All shifts are relative to the time at which the reactor reached full power and they do not account for any changes that occurred during reactor shutdowns and startups.

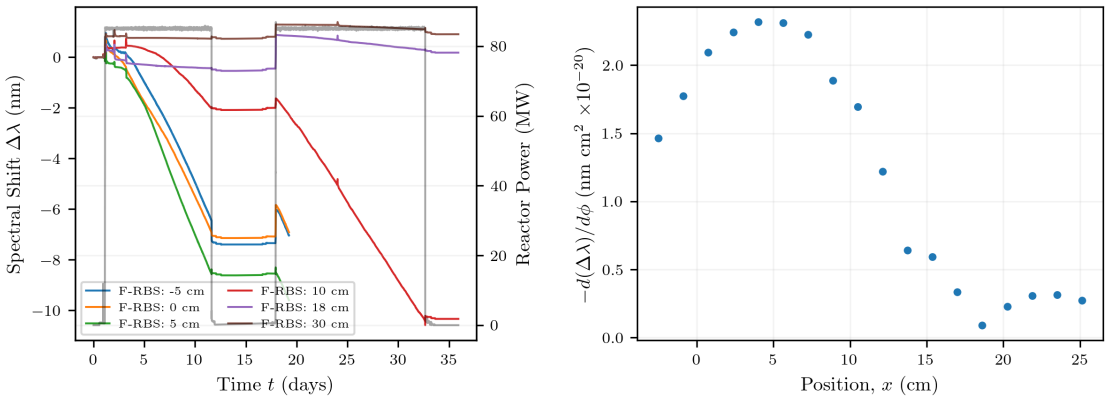

(a) Spectral shift during irradiation **(b) Drift rate by position**

Figure 9. Characterization of drift in optical fiber SF1.

combination of thermal and compaction effects for fluences $< 5 \times 10^{19}$ n_{fast}/cm^2. However, it is clear that compaction effects cannot explain the unsaturated drift that occurs at higher fluences (Figure 9a).

Larger spectral shifts that are more consistent with the SF1 data have been observed previously. The Bragg wavelength shift from a pure-SiO_2 core, F-doped SiO_2 cladding single mode fiber inscribed with FBGs and irradiated in the Massachusetts Institute of Technology Reactor (MITR) was -1 nm/day ($-d(\Delta\lambda)/d\phi = 1 \times 10^{-19}$ nm cm^2/n_{fast}) [16], which is consistent with drift rates observed in the WIRE-21 experiment (Figure 9b). Furthermore, an FBG-inscribed random air-line (RAL) fiber was included in the MITR irradiation experiment and exhibited a similar drift rate to the pure-SiO_2 core, F-doped SiO_2 cladding single mode fiber. Together, the MITR and WIRE-21 data suggest that the large spectral drift observed in irradiated a-SiO_2 optical fibers is independent of fiducial features inscribed in the fiber (e.g. FBGs) and fiber composition (e.g. pure a-SiO_2 core, RAL, etc). The large-magnitude observed spectral drift is hypothesized to be related to irradiation effects in the optical fiber coating, which is strain-coupled to the a-SiO_2. However, additional data is required to characterize this phenomenon further and is beyond the scope of the present work.

2.3 FIBER BRAGG GRATING SENSORS

Four optical fibers inscribed with Bragg gratings were included in the WIRE-21 experiment (Table 1). The SF3 and SF4 fibers used a F-doped SiO_2 core and cladding and were inscribed with 9 and 6 Type II gratings, respectively. SF5 was a pure SiO_2 core, F-doped SiO_2 cladding fiber with 28 Type II gratings and SF6 was a low bend loss fiber with UV gratings. In the present work, SF3 and SF4 were essentially replicates and are discussed together, whereas SF5 and SF6 were different fiber types inscribed with FBGs created using different techniques.

The FBGs inscribed in SF3 and SF4 remained relatively prominent in the OFDR data throughout the entire irradiation, as shown in Figure 10. All measurements shown in this figure were made while the reactor was not operating to separate the effects of radiation from the effects of temperature. Although the reactor was not operating when each of these scans were made, it is possible that vibrations from the reactor coolant pumps may have affected the scans at BOC 1, in which the FBGs are not as prominent. The intensities near the core centerline (0 cm) decreased during the beginning of Cycle 498 (BOC 1). By the middle of cycle 1

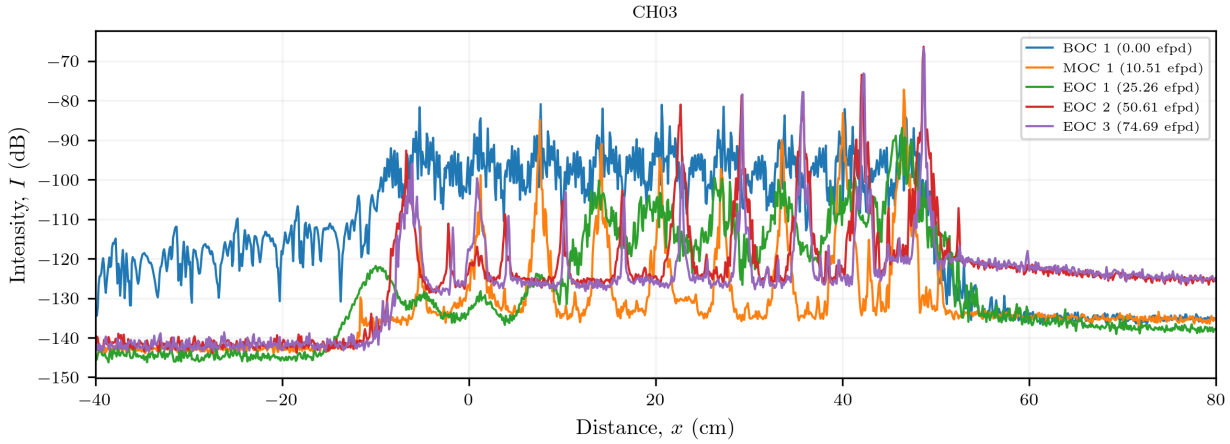

(a) SF3

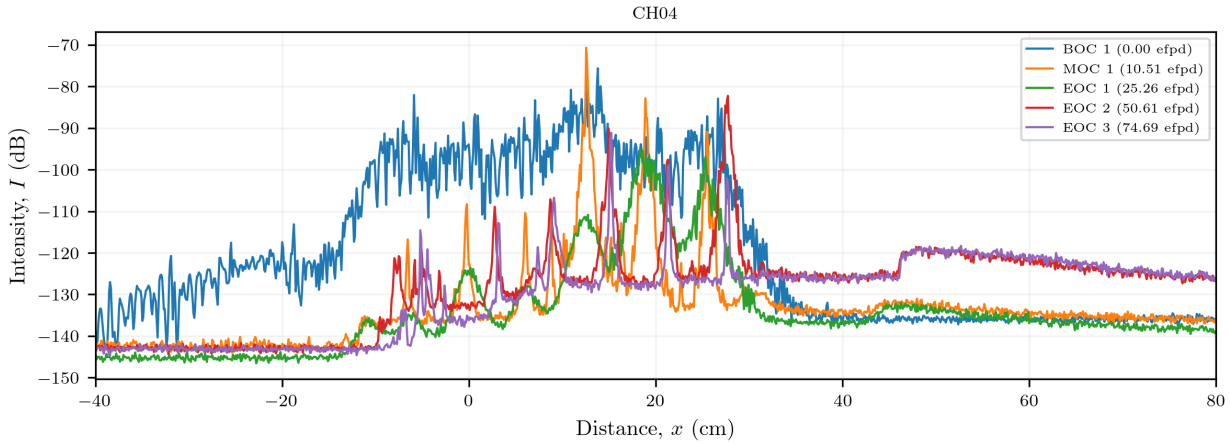

(b) SF4

Figure 10. Optical frequency domain reflectometry (OFDR) profile of SF3 and SF4 over HFIR cycles 498 (Cycle 1).

(MOC 1), the individual gratings became more prominent, relative to the RBS from the regions between gratings which appeared to equilibrate to -130 dB. By the end of Cycle 1 (EOC 1), the grating intensities decreased significantly, particularly near the core centerline.

During cycles 1 and 2, optical attenuators were placed in line with SF3 (-5 dB), SF4 (-5 dB), and SF5 (-10 dB) to prevent the FBG peaks from saturating the OBR detectors. After the measured intensities were reduced during the first two HFIR cycles, the attenuators were removed from SF3 and SF4. This explains why the intensities increased from EOC 1 to EOC 2. The attenuator was removed from SF5 earlier, following the completion of cycle 498a.

The spectral response of the FBGs in SF3 and SF4 was tracked at two locations: the FBG located nearest to the core centerline (0 cm), and at the FBG furthest above the core, located at 46 cm for SF3 and 27 cm for SF4 (Figure 11). Because the FBGs were all inscribed with the same nominal Bragg wavelength of ~1550 nm, there is often interference from neighboring peaks that complicates the tracking of spectral shifts at

one location. Therefore, it is difficult to make precise statements regarding spectral shifts at various locations. Nevertheless, the FBGs located furthest above the core centerline (Figure 11a,c) generally show much smaller peak shifts, relative to the peak locations at the start of the irradiation, compared to the FBGs located closer to the core centerline (Figure 11b,d). The shifts in the FBGs located further from the core centerline are generally in the range of 1 to 2 nm. Closer to the core centerline, peak-to-peak spectral shifts greater than 20 nm are evident (Figure 11b,d). In fact, it appears that the FBGs start to shift outside the spectral range of the OBR with increasing irradiation time, which is why data are not shown beyond 16.47 d.

The peaks from the FBG inscribed in SF3 at the core centerline appear to show a monotonic decrease in peak location after the initial increase at 1.74 d, which was likely caused by the increase in temperature during reactor startup. The peaks at 12.46 d and 16.47 d appear at much higher wavelengths, but these peak locations are non-physical and the error may have to do with the fact that the peaks are shifting outside the range of the OBR, as evidence by the appearance of tails from a peak that are evident near 1530 nm. The general trends are somwhat similar for SF4 but the monotonic decrease in FBG wavelength is not as apparent. This could be related to the fact that the spectral peaks in SF4 are less prominent. The apparent monotonic decrease in FBG wavelength, at least for SF3, is in good agreement with the RBS spectral shift measurements from SF2 through Cycle 498 (EOC 1). Similar trends were observed in the second and third irradiation cycles at locations further from the core centerline. At least some of the FBGs could be tracked throughout the course of all three HFIR cycles, or until they appear to drift outside of the 42 nm range allowed by the tunable laser configuration set in the OBR-4600 instrument.

Much like SF3 and SF4, the optical intensities in SF5 outside of the FBGs decreased but appeared to stabilize at -130 dB by EOC 1, after the in-line attenuator was removed (Figure 12). In contrast to SF3 and SF4, the FBGs in SF5 appear to disappear by EOC 1, at which point the intensities are close to the baseline value of -130 dB, even at locations where gratings were originally inscribed. Interestingly, there appears to be subtle evidence of some of the FBGs reappearing at EOC 2 and EOC 3, but ultimately the magnitude remains low. The origins of the relatively large peak that is evident near 8 cm at EOC 2 and EOC 3 are unclear. There is no reason why an FBG located at this location would have a higher peak intenstiy compared to FBGs located further above the core. It is possible that this peak is actually the Fresnel reflection that occurs between the coreless termination fiber and the end of the sensing fiber. This peak was originally in the range of -5 to -10 cm at the start of the irradiation. It is possible that the large spectral shift is caused by a compressive mechanical strain that could cause the Fresnel reflection peak to move to the right in the intensity vs. distance plots. Finally, even after the FBGs reappear at EOC 2 EOC 3, the intensities within the grating region of SF5 continue to decrease and approach the the noisefloor of the OFDR instrumentation around -140 dB. The way the intensities decrease moving from right to left (toward the core centerline) suggests that the intensity reductions are a result of increased attenuation in the fiber.

The FBG inscribed in SF5 that was located furthest from the core centerline (20 cm) survived the first HFIR irradiation cycle to EOC 1 and was analyzed to determine its spectral shift. At 20 cm on SF5, this grating exhibits an initial increase in wavelength, likely caused by increasing temperatures during reactor startup (Figure 13). At later times, the peak wavelength shifts to the left (lower wavelengths) over the three irradiation cycles, with the amplitude of the FBG peak decreasing with increasing neutron fluence. This drift is comparable with the drift at similar positions (18 cm) in SF2 (Figure 9a), further suggesting that the mechanism responsible for this spectral drift is independent of FBG feature and fiber composition.

SF6 was a singlemode fiber with a Ge-doped SiO_2 core that was inscribed with UV FBGs (Type I). These

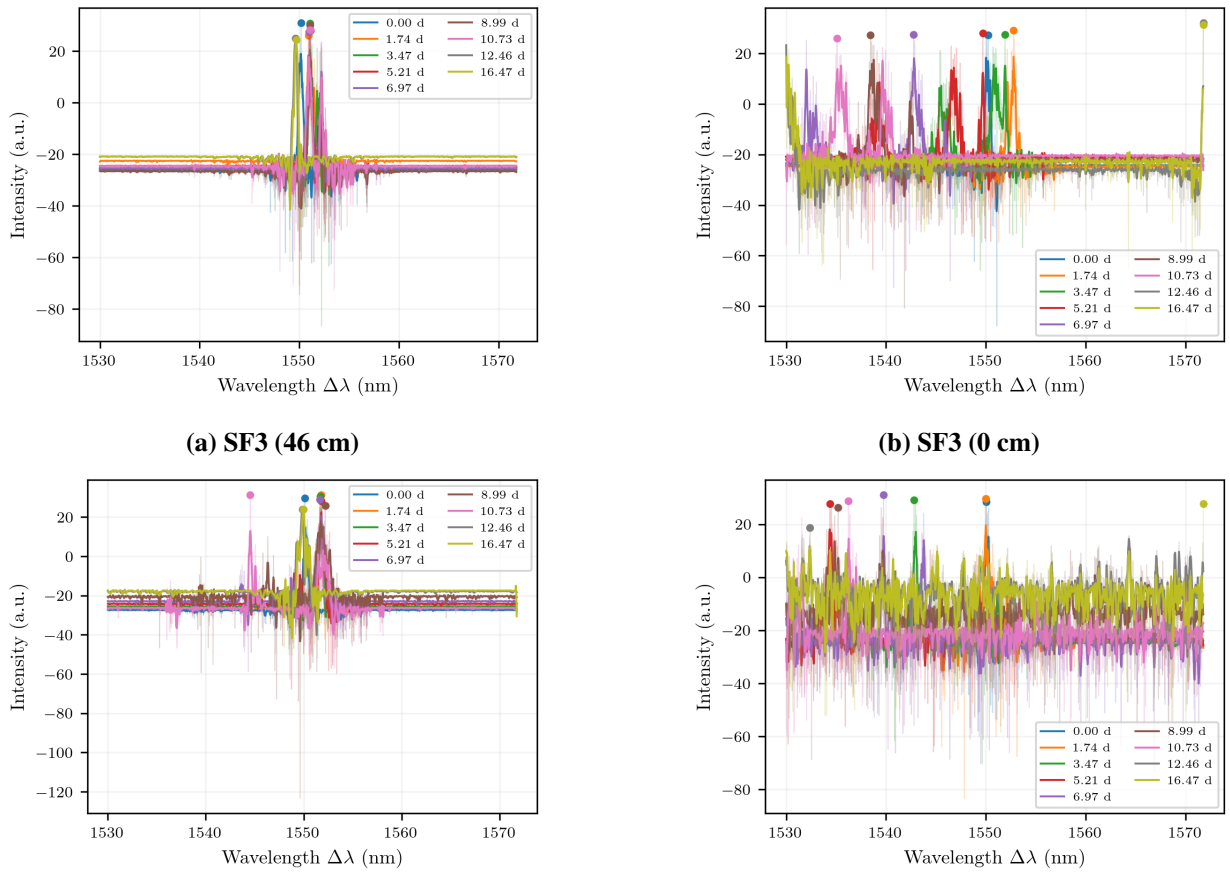

(a) SF3 (46 cm)

(b) SF3 (0 cm)

(c) SF4 (27 cm)

(d) SF4 (0 cm)

Figure 11. OFDR spectral analysis of SF3 and SF4 over HFIR cycles 498 (Cycle 1) at the location of the FBGs at the core centerline (0 cm) and the FBG highest above the core centerline (46 cm for SF3 and 27 cm for SF4).

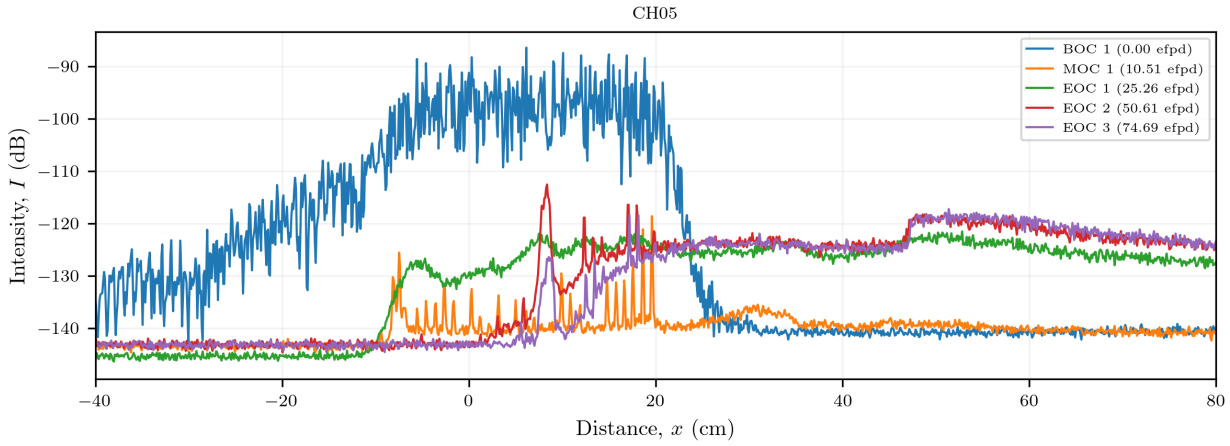

Figure 12. Optical frequency domain reflectometry (OFDR) profile of SF5 over HFIR cycles 498 (Cycle 1).

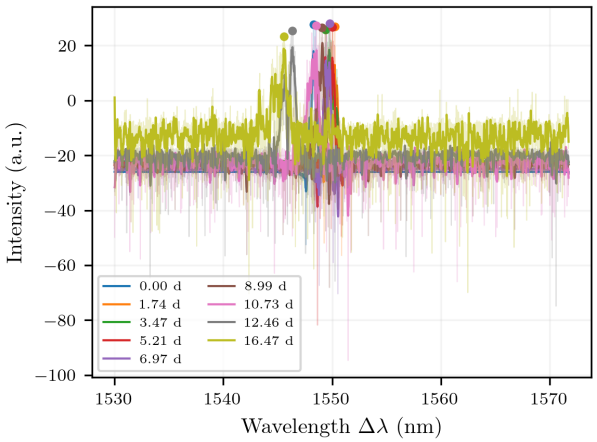

Figure 13. OFDR spectral analysis of SF5 over HFIR cycles 498 (Cycle 1), 499 (Cycle 2), and 500 (Cycle 3) at the location of the FBG highest above the core centerline (20 cm).

gratings were quickly destroyed within 2 d of irradiation in HFIR (BOC 1 in Figure 14), even at locations as far as 60 cm above the core centerline. This suggests that Type I gratings are particularly susceptible to radiation damage (both γ and neutron radiation), more so than the Type II FBGs, in the a-SiO_2. The intensities were reduced to values closer to -120 dB by MOC 1. Continued irradiation further decreased the intensities near the core centerline (0 cm), which decreased to the -140 dB noise floor by EOC 2. Interestingly, although the UV gratings between 20 and 60 cm were quickly annihilated, the intensities in this region remained in the range of -120 dB through EOC 3. This is quite different than what was observed in SF2, which included a Ge-doped SiO_2 core without Type I FBGs. SF2 showed much lower intensities (-130 dB) at positions >40 cm that decreased to the noise floor closer to the core centerline (Figure 7b). Therefore, it appears that the Type I FBG inscription process allows the Ge-doped fiber to retain a higher backscattered intensity even after the FBGs are destroyed.

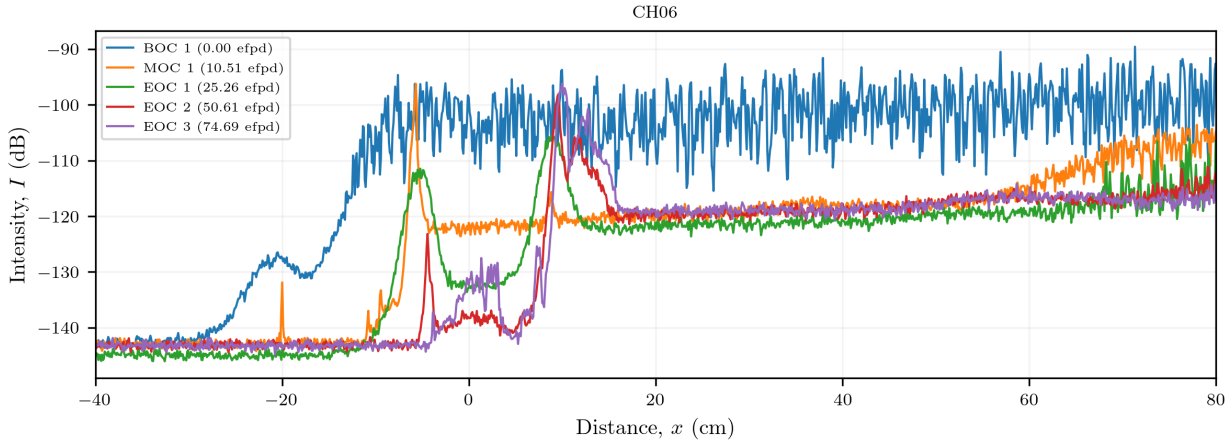

Figure 14. Optical frequency domain reflectometry (OFDR) profile of SF5 over HFIR cycles 498 (Cycle 1), 499 (Cycle 2), and 500 (Cycle 3).

Because the FBGs that were located within 60 cm of the core centerline were destroyed so quickly and the FBGs further above the core survived, it was difficult to resolve spectral shifts within the core region. The gratings that did survive had such a strong spectral signature that they dominated the spectral response even after filtering to analyze sensor gauge regions closer to the core centerline.

2.4 HOLLOW CORE FIBERS

The two remaining fibers–SF7 and SF8–were hollow-core fibers (HCFs) spliced directly to the lead-in fiber and terminated with a 15 cm segment of pure SiO_2 core, F-doped SiO_2 cladding fiber (Table 1). The difference in the refractive index of core of the HCFs and the lead-in fiber generated large Fresnel reflections at approximately 65 and 75 cm above the core centerline for SF7 and SF8, respectively (Figure 15). A second Fresnel reflection occurred between the end of each HCF and the termination fiber, initially at -10 and -5 cm for SF7 and SF8, respectively. Notably, the initial OFDR measurements of SF7 and SF8 appeared similar: a 76 cm segment of HCF bracketed by two Fresnel reflections. During irradiation, SF7 exhibited a decrease in intensity with increasing neutron fluence for positions between -10 and 20 cm. At positions > 20 cm, the intensities remained approximately constant near -110 dB over all three irradiation cycles ((Figure 15a). In contrast, SF8 showed intensities that decreased to the noise floor (-140 dB) over most of the HCF region (Figure 15b).

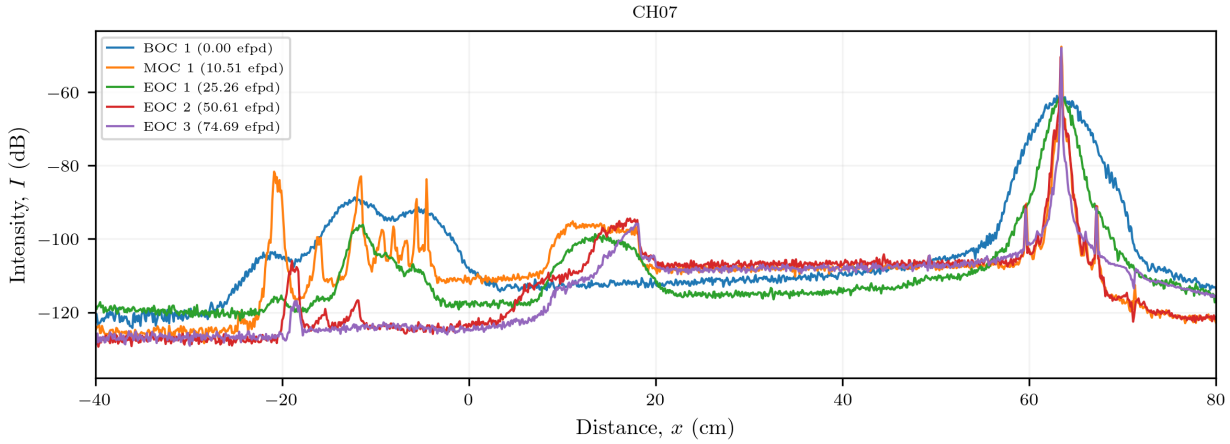

(a) SF7

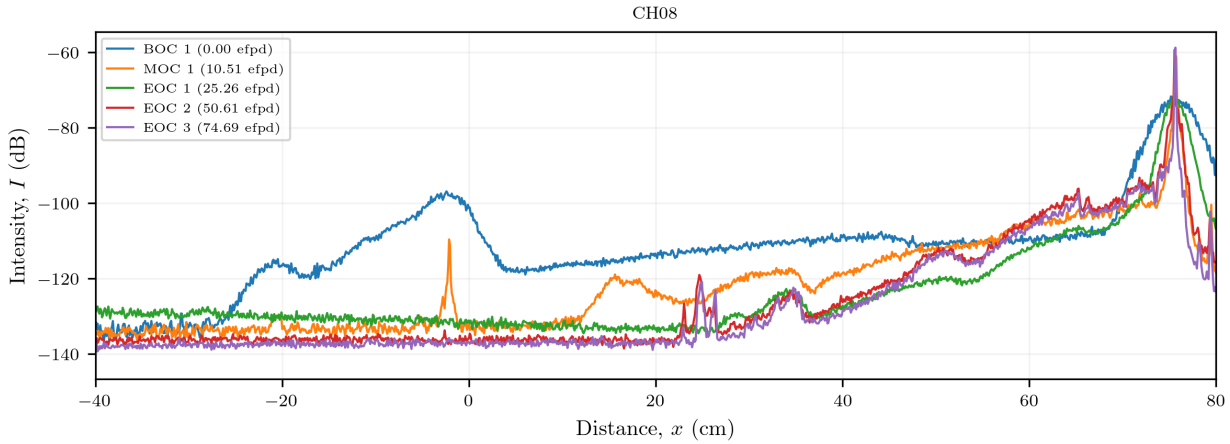

(b) SF8

Figure 15. Optical frequency domain reflectometry (OFDR) profiles of SF7 and SF8 over HFIR cycles 498 (Cycle 1), 499 (Cycle 2), and 500 (Cycle 3).

The changes in intensity in SF7 and SF8, particularly around the core centerline, indicate that HCFs is susceptible to degradation as the fast neutron damage accumulates. However, it should be noted that the optical fibers in WIRE-21 were interrogated using OFDR, which only provides an indication of reflectivity magnitude. HCFs may still provide benefits for optical transmission, but additional experiments using a double-ended test (sending and receiving of light) are required to investigate this.

3. SELF-POWERED NEUTRON DETECTORS

The WIRE-21 experiment also included SPNDs at four different elevations across the HFIR beryllium reflector to perform real-time neutron flux measurements during reactor operation. These elevations correspond to +15, +5, -5, and -15 cm relative to the HFIR midplane, as shown in Figure 16. SPNDs are adept at providing unperturbed neutron flux measurements in an operating reactor because of their compact geometry which can be incorporated into reactor coolant channels, or in this case, experiments with small internal volumes. SPNDs also have a simple, robust detector geometry capable of high-temperature operation and do not require external power for operation. To the authors' knowledge, this was the first SPND measurement of neutron flux in the history of HFIR. Signals were recorded directly from SPND leads using a picoammeter and also using a custom fabricated preamplifier designed to compensate gamma-induced signals in the detectors. Of the four SPNDs, only one (SPND-D) appeared to operate properly and consistently during the course of the experiment, whereas the others were either damaged prior to reactor operation or failed during operation. Measurements from the SPNDs during three HFIR irradiation cycles are presented in the following sections. Particular focus is directed at reactor power transients, as well as temperature transients which produced signal fluctuations in the SPNDs. A calculation of the detection sensitivity of SPND-D using modeled neutron flux intensities in the experiment is also included.

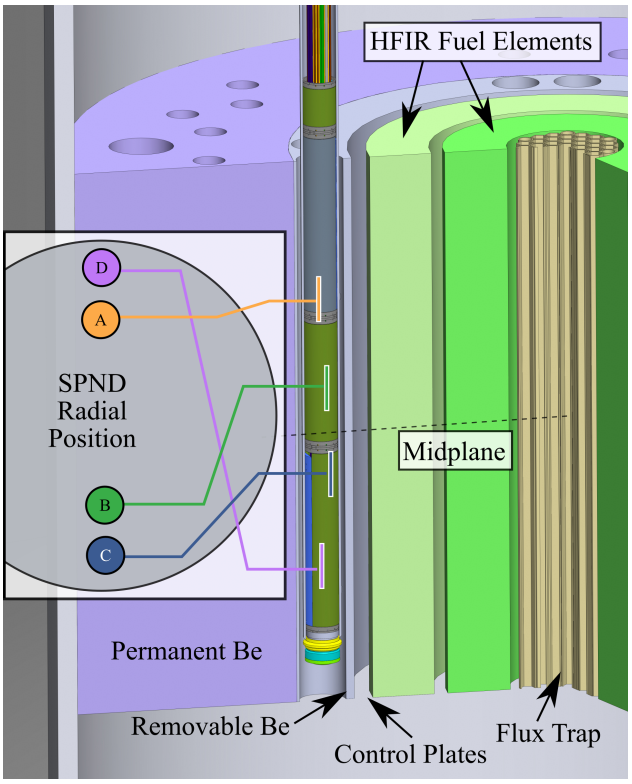

Figure 16. Radial and axial locations for SPNDs in WIRE-21. Inset figure is a cross-sectional view of the experiment with the radial position of each SPND.

3.1 THEORY

SPNDs operate on the principle of radioactive decay (prompt or delayed) following neutron capture in a material. In this work, SPNDs were fabricated using V metal as the emitter material, MgO as the insulator, and Inconel 600 as the outer sheath and internal lead wires. The vast majority, approximately 99%, of the neutron induced signal produced by V is delayed, generated through neutron absorption and beta particle emission. Vanadium is primarily composed of V-51 (99.75%), which emits a prompt gamma ray (1.43 MeV) following thermal neutron capture (σ_C=4.9 b). V-52 subsequently undergoes beta decay with a half-life of 3.74 minutes (224 s) and a mean energy of 1.07 MeV. The small (1%) prompt response in V caused by prompt gamma emission is neglected in this analysis. Beta particles from the emitter are ejected isotropically into the surrounding dielectric material, which is usually arranged coaxially with the emitter. Particles with sufficient energy to overcome the space-charge region established in the insulator travel to an electrically conductive outer sheath called *the collector*. This process generates a net electrical current between the emitter and the collector, which can be given by

$$I_0 = kN\sigma_C\Phi e, \tag{12}$$

where k is a detection efficiency factor, N is the number of target nuclei in the emitter, σ_C is the capture cross section of the target isotope, Φ is the local neutron flux in the vicinity of the detector, and e is the elementary charge. Detection efficiency depends upon several factors, including the branching ratio of the primary reaction, neutron self-shielding, emitter and collector geometry, and characteristics of the space-charge field established in the dielectric region. Local neutron flux can be inferred by measuring the current generated between the emitter and the collector. Although I_0 in Eq. (12) represents the current generated in the SPND under steady-state flux conditions, a step increase in neutron flux will cause increased current following

$$I(t) = I_0\left(1 - \exp\left(\frac{-ln(2)t}{T_{1/2}}\right)\right). \tag{13}$$

A decrease in reactor power from steady state to zero causes a time varying current of the form

$$I(t) = I_0 \exp\left(\frac{-ln(2)t}{T_{1/2}}\right), \tag{14}$$

where $T_{1/2}$ is the half-life of the primary beta-emitting isotope, and t is the time following the transient.

Although SPNDs are intended to measure in-core neutron flux, the high gamma flux that typically accompanies neutrons in a reactor can cause additional interactions with the detector which can produce fast secondary electrons and contribute additional electrical signals. These additional interactions can be particularly problematic for the cable connecting the SPND emitter to external data acquisition equipment, which is more susceptible to gamma interactions along the much longer cable length. Therefore, to extract the gamma-induced component of the SPND signal, a second wire that is identical to the SPND emitter lead is included for gamma subtraction.

3.2 MODELING

A neutronics model of SPNDs in WIRE-21 was developed to determine neutron flux during a typical HFIR cycle. Modeling was performed using a simplified geometry of the experiment in the HFIRCON [17] coupled radiation transport and depletion code. HFIRCON is a collection of nuclear modeling codes, including ORNL-TN [18] for radiation transport, ORIGEN [19] for nuclide depletion, ADVANTG [20] for source biasing and variance reduction, and a suite of Python and C wrappers for data transfer and automation between codes. Representative cross sections of the SPNDs and other experiment components were subdivided into 1 cm vertical sections along the length of the reflector.

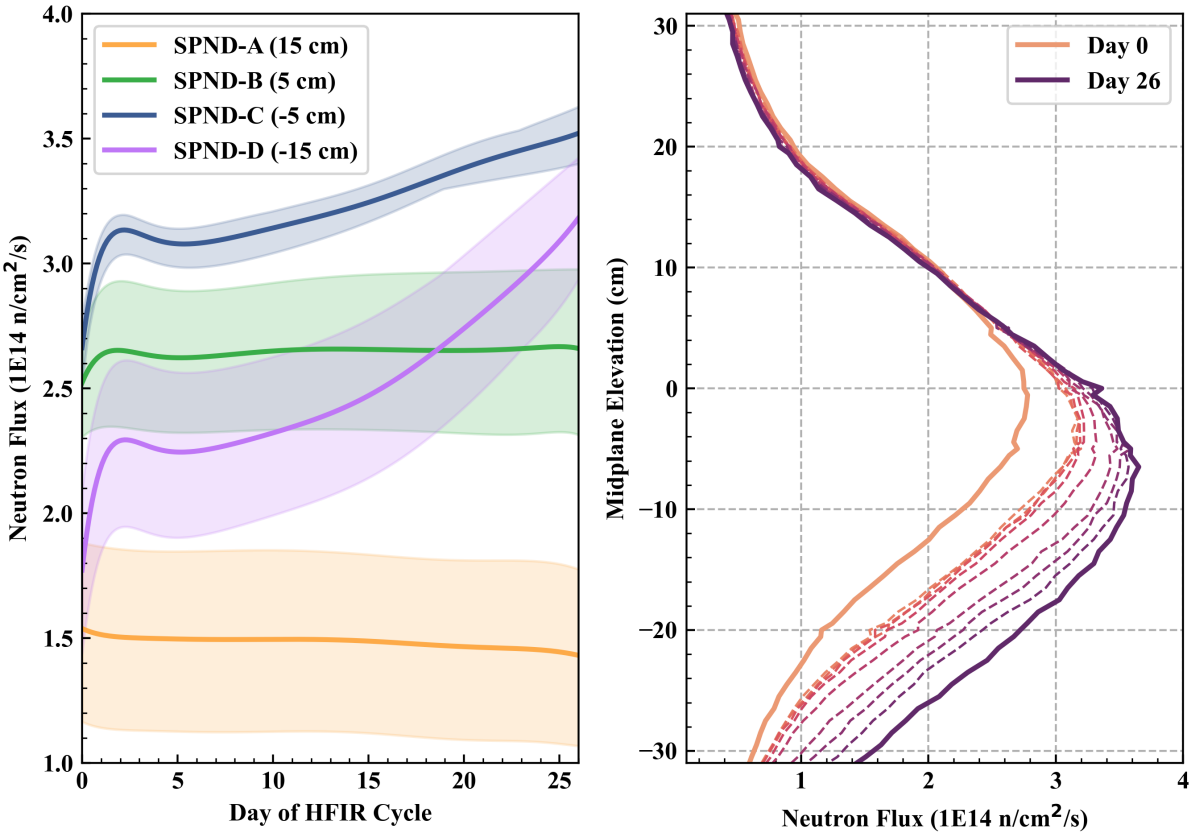

Figure 17. Modeled time-dependent thermal neutron flux for each SPND (left). Spatially dependent and time-dependent thermal neutron flux spanning reflector (right).

This model provided spatial-, time-, and material-dependent heat generation rates, neutron flux, and reaction cross sections for a typical 26-day HFIR cycle. Thermal neutron flux across the RB experiment position for each time step modeled are displayed in Figure 17 (right). As indicated in Figure 17, the peak neutron flux in the RB facility migrates from the HFIR midplane to approximately 5 cm below the midplane over the course of a cycle while also increasing in magnitude. This effect is in part caused by movement of the peak fission density, and therefore the power distribution, from the midplane to the axial ends of the core as fuel is depleted. Power density also shifts from the inner to the outer fuel element as the cycle progresses, causing increased neutron flux in the reflector that surrounds the fuel [21]. More

consequently, the movement of control plates over the course of a cycle influences the neutron flux distribution in the adjacent RB location. HFIR control plates composed of Er, Ta, and Al sections are withdrawn symmetrically away from the midplane to maintain reactor power. The control elements also overlap one another in the axial direction, placing the elements at two different radial positions relative to the core center. The RB experiment location is adjacent to the control plates and can be near highly absorbing Er or neutron transparent Al segments, depending on the control element position. The combination of these factors leads to the time-varying asymmetric flux in Figure 17(b).

Results of radiation transport modeling were used to predict thermal flux intensities in the locations of each SPND emitter as shown in Figure 17(left). Emitters were positioned in the experiment so that the midpoint of each was located as follows: SPND-A (+15 cm), SPND-B (+5 cm), SPND-C (-5 cm), and SPND-D (-15 cm). Because of the spatially varying flux profile, the neutron flux intensity changed significantly over the length of the 5 cm SPND emitter, as indicated by the shaded regions in Figure 17(left). This effect was less pronounced for SPND-C, which was located in the peak flux region of the RB, where the power profile is flatter. Modeling results for SPND-A and SPND-B, which were located above the midplane, also indicate less variability in flux magnitude over a HFIR cycle relative to SPND-C and SPND-D below the midplane. Flux values for modeled cycle days were used to determine the detection sensitivity of SPND-D during the first (498) and third (500) cycles of irradiation.

3.3 EXPERIMENTAL

3.3.1 Detectors

Low-cost, unoptimized SPNDs were fabricated by Idaho Laboratories Corporation (ILC) to the nominal dimensions shown in Figure 18. High-purity V was used as the emitter wire, which was welded to one Inconel 600 lead of a 20 m mineral-insulated (MI) cable. The electrical insulation of the MI cable and emitter region were made from compacted MgO sheathed in Inconel 600. A second Inconel 600 lead in the MI cable was terminated slightly before the V emitter to provide a gamma compensation signal in the detector. Electrical leads were twisted helically around one another approximately every 30 cm to provide noise reduction. The electrical resistance of each SPND was measured prior to experiment installation and showed a large ($> 1 M\Omega$) resistance between the emitter, collector, and gamma compensation wire. Similar resistance measurements performed after installation indicated an electrical short between the gamma compensation wire and collector caused either by damage to the detector leads or an unwanted electrical connection between signal leads somewhere between the experiment and MIF. This short was observed in the gamma compensation wire of all four SPNDs.

3.3.2 Data Acquisition

Data from HFIR systems, including thermocouples, pressure sensors, reactor power, and flow regulators, were recorded and stored in the MIF historian at a sampling frequency of 1 Hz. SPND electrical current data from Keithley picoammeters (Model 6482, 1 fA resolution) were recorded at approximately 0.48 s intervals using a LabVIEW acquisition program. Synchronizing the two data sets proved challenging because the timestamps of the MIF historian data appeared to lag the SPND timestamps by approximately three hours. As Figure 19 shows, the abrupt change in SPND current corresponds well with the SCRAM times recorded in the HFIR operation logs, whereas the reactor power recorded in the MIF historian leads the SCRAM events by approximately 3 hours. To resolve this discrepancy, the derivative of the SPND and reactor signals was used to calculate the time offset of the MIF historian and was found to be

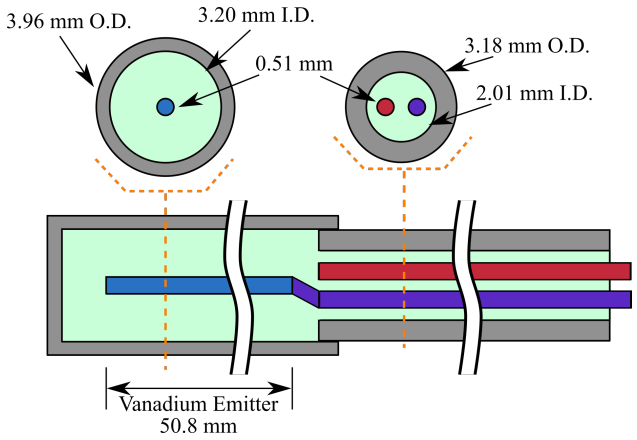

Figure 18. Nominal dimensions of SPNDs included in WIRE-21.

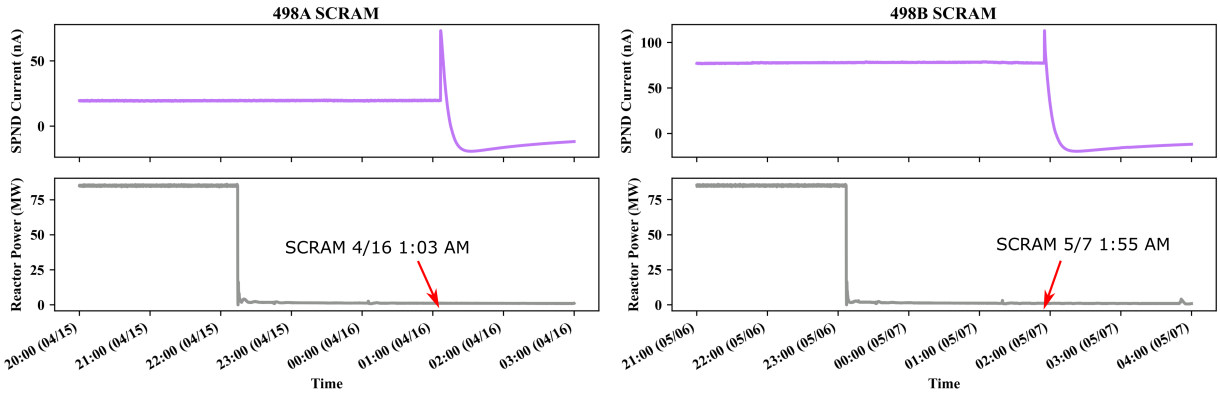

Figure 19. SPND-D signal from LabVIEW vs. reactor power level from MIF historian following two HFIR SCRAMs. SCRAM times indicated with red arrows are taken from reactor operations logs.

approximately 2:48:18 (hh:mm:ss) for SCRAMs 498A and 498B. This delay may have been caused by the MIF historian's isolation from internet connections and lack of connection to time synchronization services, leading to a divergence between GMT and the historian's internal clock.

3.4 RESULTS

3.4.1 Power Transients

The WIRE-21 experiment was assembled and placed into the HFIR RB facility in April 2022. Although HFIR normally operates continuously at 85 MWth for cycles of 25—26-days, reactor startup operations provided a unique opportunity to observe signals in the SPNDs at varying power levels. For the first cycle of operation (498), HFIR power was increased several times to 10 MWth for 30-minute intervals prior to full power. This provided low power step function changes in neutron flux to allow for observation of changes in the SPND signals, as shown in Figure 20. SPNDs -A and -D exhibited the largest response with reactor power (5-8 nA), whereas SPNDs -B and -C demonstrated an unexpectedly attenuated response (0.2-2 nA). Initial interpretation of the SPND signals was difficult to reconcile because of the unusual

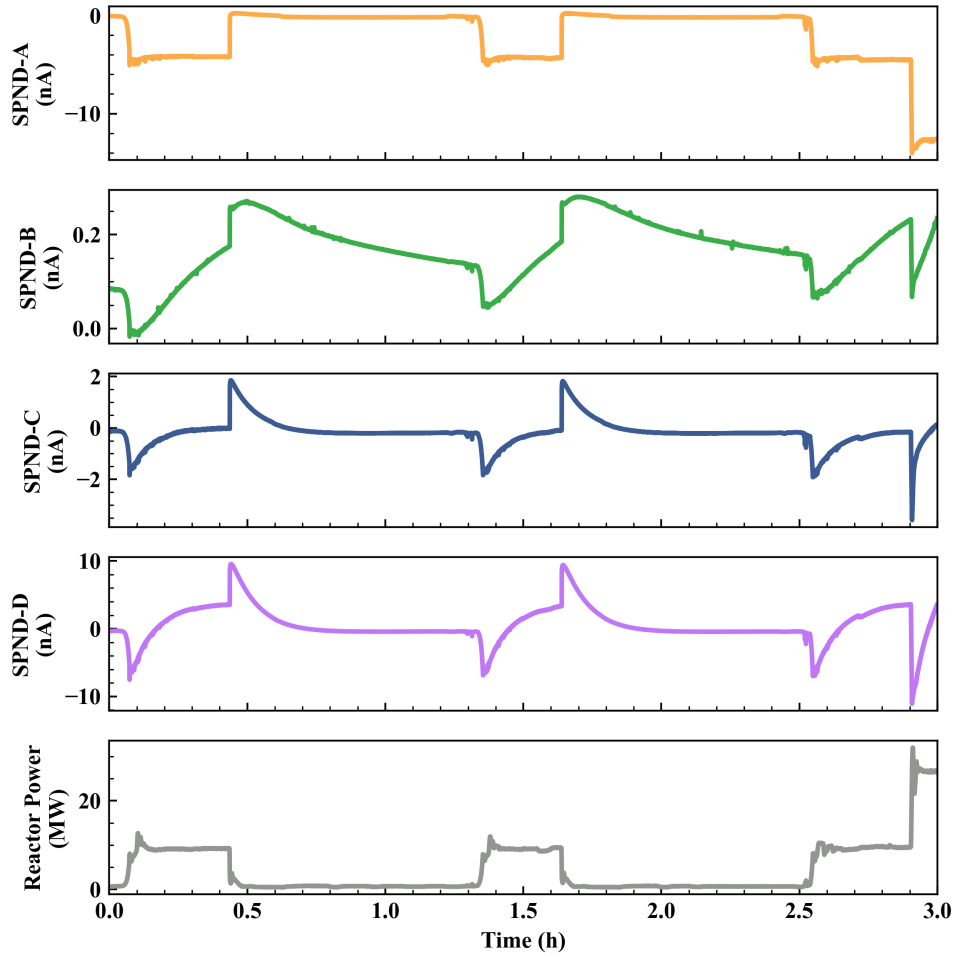

Figure 20. SPND response during cycle 498 reactor startup transients.

bidirectional progression of the SPND current with changes in reactor power. However, all four detectors displayed the same prompt decrease in signal current with a rise in power followed by an inverse response with a decrease in reactor power. Additionally, SPND-B displayed a significantly different response with respect to time compared to the other three SPNDS, showing a nearly linear yet attenuated increase in current during 10 MW power levels followed by a nearly linear decrease with the reactor shut down.

Examination of the end of the second transient of Figure 20 on a semilog scale shows the currents from SPND-A, -C, and -D decreasing exponentially (Figure 21) in accordance with Eq. (14). SPND-B displayed a significantly flatter time response, indicating that its response was caused by a different mechanism than the other SPNDs and that it may have been damaged during installation. A linear regression was performed on the natural log of each SPND's signal from 150 to 390 *s* of the same transient, shown as black lines in Figure 22. Converting the slope of each regression to half-life shows that SPND-A, -C, and -D decay with similar time constants to that seen in the 3.74 minute half-life of V-52, suggesting that the signal is caused by decay in the V emitter.

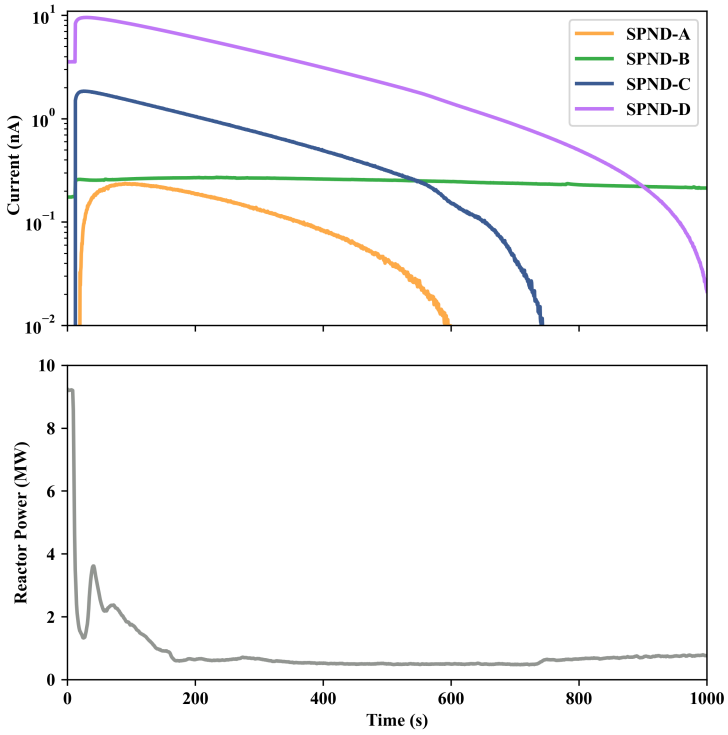

Figure 21. SPND signals following 10 MW transient on semilog scale.

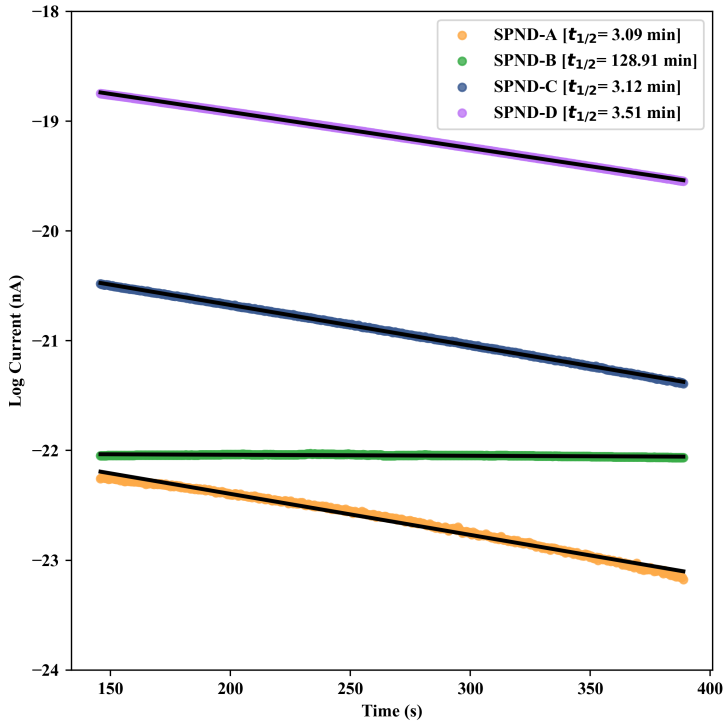

Figure 22. Linear regression of 240 s window of SPND signals (Figure 21) following 10 MW transient; decay constants shown in figure inset.

3.4.2 Signal Curve Fitting

To unfold aspects of the SPND time-varying response, each signal was curve-fitted using a linear-least-squares algorithm to a sum of exponential functions of the form:

$$I(t) = A + Be^{pt} + Ce^{qt}. \tag{15}$$

Results of this curve fit following the two reactor power decreases from 10 MW at 0.4 and 1.6 hours (Figure 20) are shown in Figure 23, with 0 seconds representing the end of 10 MW power time interval. Curve fitting was not performed on SPND-B because this signal did not yield real coefficients to Eq. (15), and as previously mentioned, it was likely damaged. As Figure 23 indicates, the SPND signal is well represented by the sum of two exponential functions with a short half-life and moderate half-life. The two exponential functions were also found to contribute to the signal with the opposite sign, with the moderate half-life having a positive contribution and the short half-life producing a negative contribution.

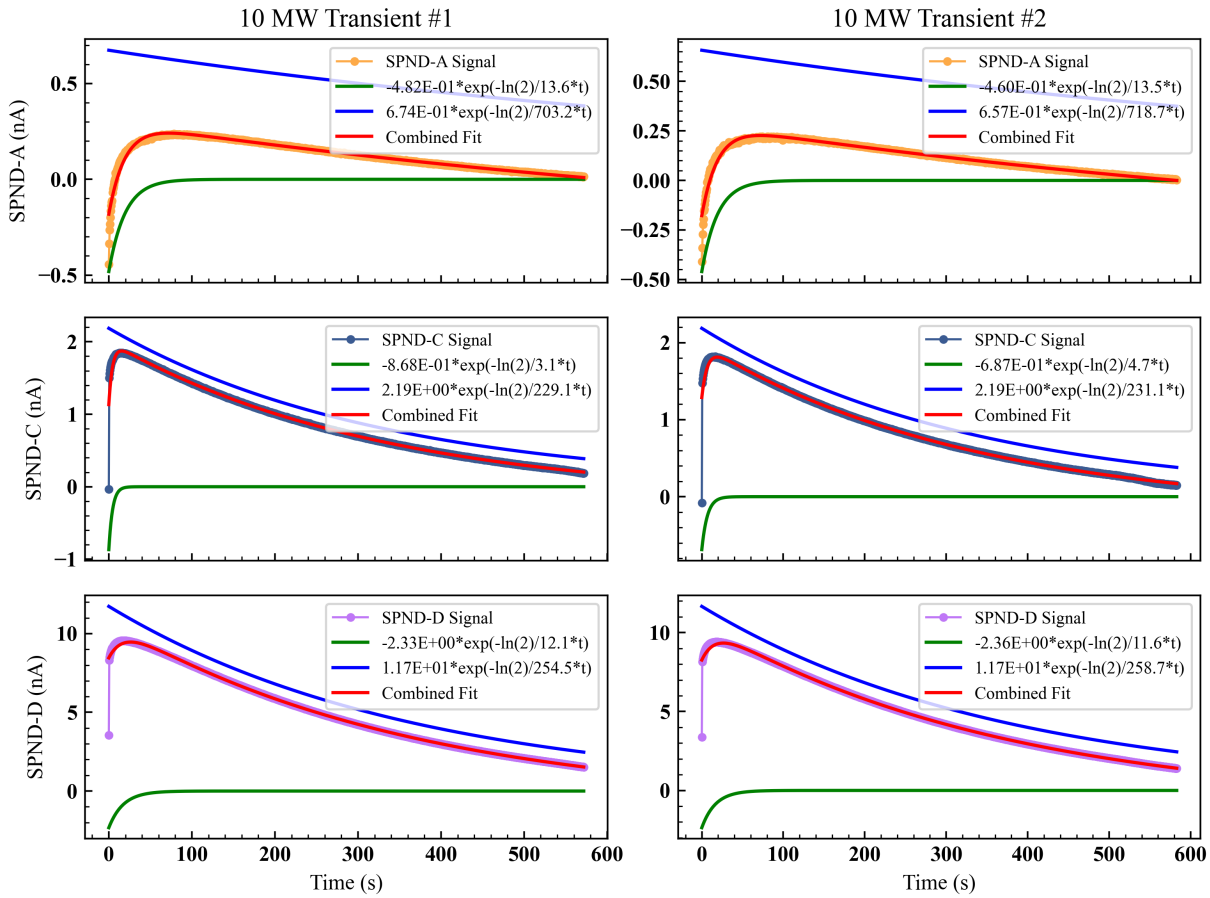

Figure 23. Exponential curve fitting of SPND-A, -C, and -D for two 10 MW reactor transients.

Coefficients of best fit are included in the equations in the legend of each graph, with the exponential term converted to half-life ($q, p = -ln(2/T_{1/2})$. The exponent coefficients converted to half-life for the fit curves

(blue) in SPND-C (229.1 and 231.1 s) and SPND-D (254.5 and 258.7 s) once again correspond well with the 224 *s* half-life of V-52, indicating that the observed signal is caused by V-52 beta decay in the detector. The second exponential curve (green) yielded significantly smaller (3.1–12.1 s) half-life coefficients with an opposite contribution. This suggests that the moderate decay signal is caused by V-52 decay, as shown in Eq. (14), whereas the prompt response is caused by another mechanism. The most likely source of the prompt contribution may be photoelectron interactions with prompt fission photons or fission product decay photons from HFIR's fuel during power operation generating a current in the opposite polarity of current generated by neutron absorption in the SPND emitter. This effect was present in all four SPNDs, with changes in current inversely proportional to reactor power.

Curve fitting for SPND-C and SPND-D signals during an increase to 10 MW power yielded similar results, with exponent coefficients close to the half-life of V-52 and following the form of Eq. (13). Although SPND-A did not yield exponent coefficients in close agreement with the 224 s half-life of V-52, the total signal of this detector was quite small ($\approx$ 2.5 nA), which makes deconvolution more challenging. The reason for the SPNDs' bipolar behavior is unclear, but it could be caused by the gamma compensation wire being electrically connected to the collector. The relatively thick sheath of the collector relative to other SPNDs presented in the literature could also provide a larger mass for gamma interactions in the cable, thus causing a signal of opposite polarity to the emitter signal.

3.4.3 Gamma Compensation with Custom Preamplifier

A custom preamplifier was designed to subtract gamma compensation wire current from the emitter wire current and was used for the second cycle of irradiation (499). In this configuration, the electrical current measured in the MIF should correspond to the signal from neutrons only. Figure 24 shows the recorded signal from the preamplifier for all four SPNDs. SPND-D, which had the largest response to neutrons during the first cycle of irradiation (Figure 21), appeared to be truncated by the gain limits of the preamplifier for the entire cycle. This was likely caused by underestimating the expected SPND signal when designing the preamplifier and selecting electronic components based on these expectations. Because the preamplifier was located as close to the experiment as possible to improve signal-to-noise ratio, gain adjustments could not be made while the reactor was operating. Future designs should enable remote adjustment of the preamplifier gain if possible, or the preamplifier should be placed in a more accessible location. SPND-B appeared to be truncated by the lower limit of the preamplifier, but the earlier analysis suggests this SPND was likely already damaged. SPND-A remained within the limits of the preamplifier, as did SPND-C at various points. However, because the gamma compensation wire was electrically connected to the SPND collector, the preamplifier was not subtracting the correct gamma compensation current, so interpretation of these results is uncertain. However, SPND-A and -C did demonstrate some expected behavior, such as an exponential signal decay at the end of cycle, although this was significantly more attenuated than expected.

3.4.4 Temperature Response

Temperatures in WIRE-21 were manipulated during steady-state reactor operations to observe the response of other sensors included in the experiment. This was achieved by adjusting the Ar concentration of sweep gas flowing to the experiment, which has the net effect of decreasing thermal conductivity of small gaps between internal components and the experiment housing in contact with the HFIR coolant. As shown in Figure 25, the temperature transient had an immediate and proportional effect on the signals of SPND-C and SPND-D, which were located at -5 cm and -15 cm below the HFIR midplane, respectively, despite no

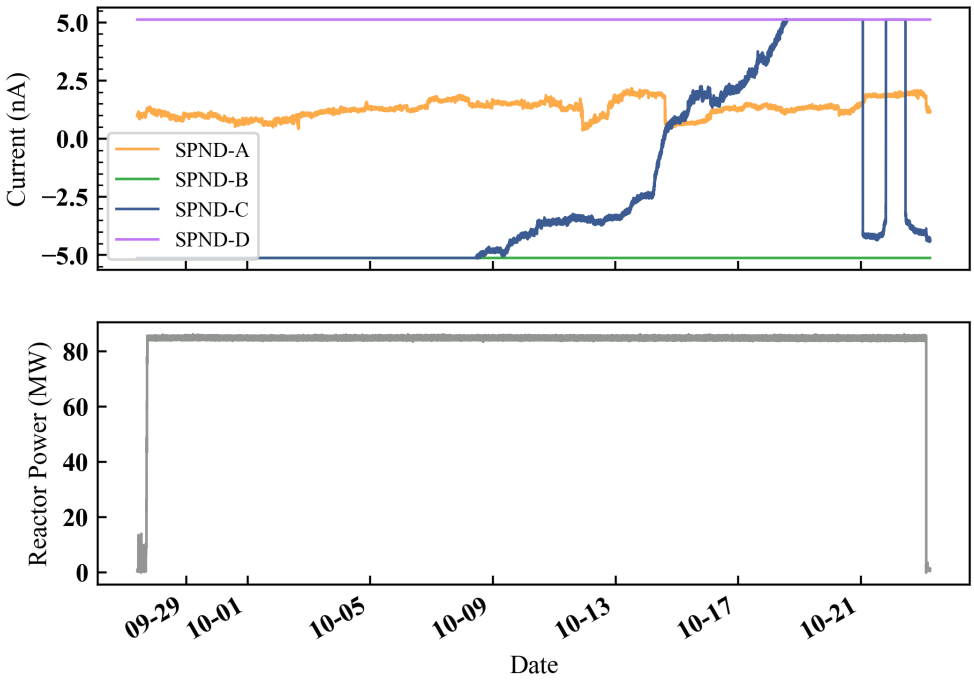

Figure 24. SPND measurements from cycle 499 using preamplifier gamma subtraction.

changes in reactor power. However, the response of each SPND was different, with SPND-C increasing in proportion to temperature, whereas SPND-D showed an inverse relationship.

A temperature response in the SPNDs was expected, because the SPND signal actually indicates the neutron interaction rate—not the neutron flux directly. Previous work [22] has shown that the weighted absorption cross section of V-51 in a Maxwellian neutron flux distribution has an inverse cubic dependence on absolute temperature, decreasing with increasing temperature. This trend is observed in SPND-D (Figure 25), with decreasing current when the local temperature increases despite no changes in reactor power. The increased temperature of the experiment could be perturbing local neutron flux above thermal energies, thus resulting in a reduced average capture cross section as predicted by Moreira. The signal from SPND-C has the opposite trend, increasing the output signal when the temperature increases. Although the explanation for this could be Doppler broadening of resonance integrals in the V-51 cross section, the very low signal produced by SPND-C during other times of the irradiation suggests that it may have been damaged and not functioning properly.

3.4.5 SPND Sensitvity

Signals from SPND-D were plotted for cycles 498 and 500, Figure 26, to analyze the SPND response following two HFIR cycles. SPND-D was chosen for a sensitivity calculation as this was the only SPND which appeared to operate consistently during these two HFIR cycles. SPND data between day 2 and 7 was somehow lost for cycle 500; however, SPND data for other times in the cycle appeared normal. Coincidentally, cycles 498 and 500 both experienced a SCRAM during the tenth day of operation, as indicated by the abrupt increases in SPND signals. The same general trends were displayed in cycle 498

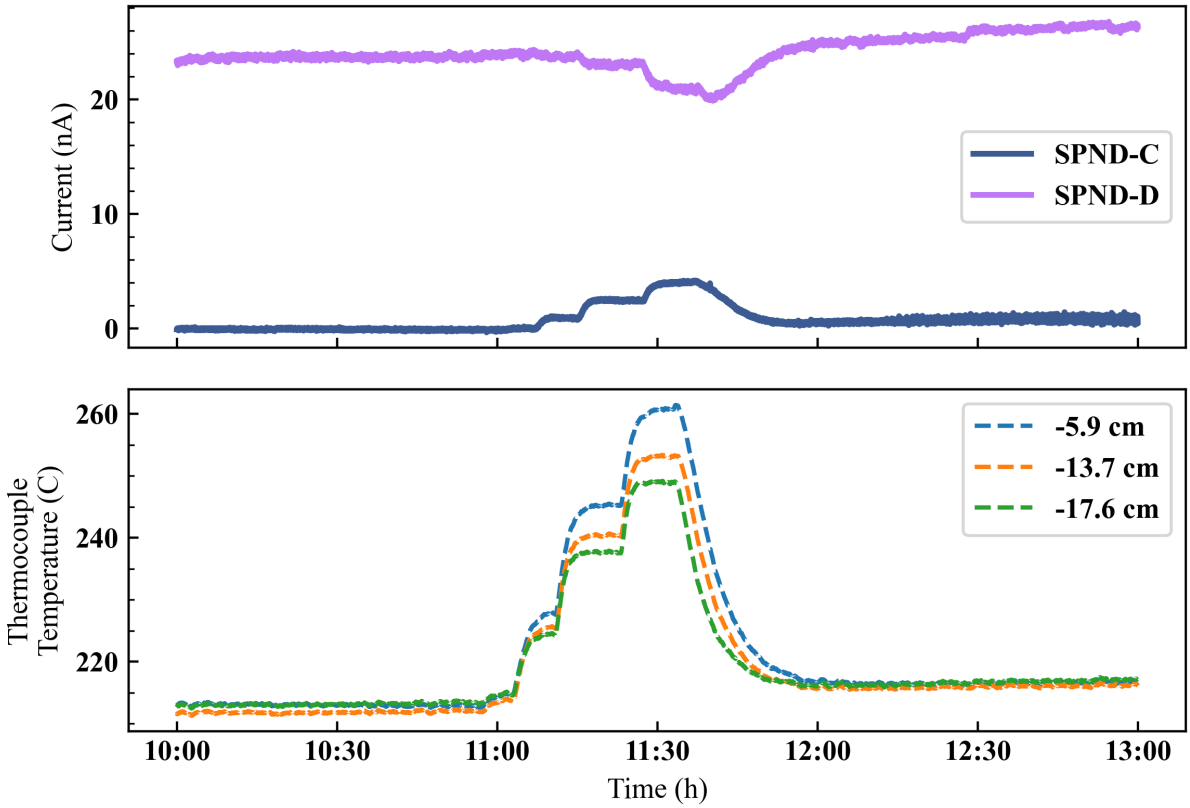

Figure 25. SPND-C and -D signal response to temperature manipulation during reactor operation.

and 500, including 1.) a sharp decrease in SPND current shortly after reaching full power on day one, 2.) a rise in current over the next two days followed by a decrease (although data is missing for cycle 500), and 3.) a steadily increasing signal for the remainder of the cycle. These trends also match, heuristically, the modeled neutron flux for SPND-D in Figure 17.

To determine the neutron sensitivity of SPND-D, the measured current was tabulated at the same time intervals used in the neutronics modeling. The SPND signals at each time interval were averaged over 5 minutes and divided by the modeled neutron flux intensities, thus yielding the experimental neutron sensitivities shown in Table 2. The calculated sensitivities for cycles 498 and 500 also follow the same general trends, decreasing in the middle of the cycle but trending higher at the beginning and end of the cycle. The cycle-averaged sensitivities were determined to be 1.5×10^{-22} and 1.4×10^{-22} $A/n\nu$ for cycles 498 and 500, respectively. This is reasonable, or slightly lower if normalized to the 5 cm emitter length, when compared to other values for V SPNDs available in the literature. This estimate does not include gamma compensation in the detector because the gamma compensation wire was unexpectedly shorted to the collector and thus provided no signal. The change in sensitivity between cycles corresponds to a 6.5% decrease, which is larger than the expected burnup of 2% following two cycles of irradiation. However, the significant fast flux in this region of the reactor could also be transmuting V, contributing to the faster-than-expected depletion.

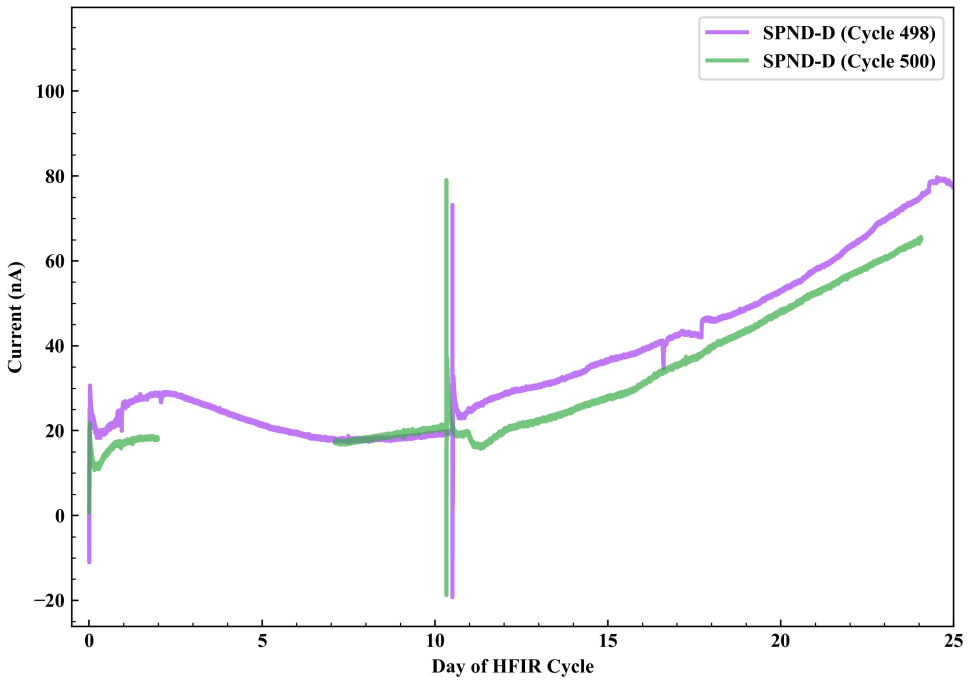

Figure 26. SPND-D signal from cycles 498 and 500 overlaid for comparison.

Table 2. Measured SPND-D current for specific days of HFIR cycles 498 and 500, along with modeled neutron flux and SPND sensitivity.

Day of cycle	Measured current (nA) Cycle 498	Measured current (nA) Cycle 500	Modeled neutron flux $(n/cm^2/s)$	Sensitivity $(A/nv \times 10^{-22})$ Cycle 498	Sensitivity $(A/nv \times 10^{-22})$ Cycle 500
0	29.1	20.4	1.77×10^{14}	1.6	1.2
1	26.3	17.0	2.19×10^{14}	1.2	0.8
3	26.9	—	2.28×10^{14}	1.2	—
5	21.3	—	2.25×10^{14}	0.9	—
10	19.1	20.5	2.33×10^{14}	0.8	0.9
15	36.7	27.8	2.48×10^{14}	1.5	1.1
20	52.8	48.2	2.75×10^{14}	1.9	1.8
22	63.5	56.7	2.88×10^{14}	2.2	2.0
24	74.8	65.0	3.02×10^{14}	2.5	2.1

4. SUMMARY & CONCLUSIONS

The WIRE-21 experiment was designed, fabricated, and irradiated in the HFIR reflector in 2022 as a multipurpose experiment to test several nuclear sensing technologies. The experiment was irradiated for three full HFIR cycles and contained a variety of nuclear instrumentation, including four V-emitter SPNDs, several silica fiber optic distributed temperature sensors, SiC passive temperature monitors, neutron activation flux wires, and two inductively coupled wireless temperature and pressure sensors developed by WEC. Active sensors and gas lines in the experiment were connected to the adjacent MIF for monitoring

and control during irradiation. Analysis of measurements from the SPNDs during the first cycle of irradiation demonstrated that three of the four SPNDs behaved as expected during reactor power transients. SPND-B (-5 cm) appeared broken shortly after reactor startup in the first cycle. SPND-D (-15 cm) was the only detector to exhibit a reasonable signal response during all cycles. Gamma compensation wires in the SPNDs were found to be electrically shorted to the collector which could account for the unusual bipolar transient behavior observed. A radiation transport model of the experiment created using HFIRCON was used to calculate the neutron flux that was used for determining the sensitivity of SPND-D. Results showed an average sensitivity of 1.5×10^{-22} and 1.4×10^{-22} $A/n\nu$ for cycles 498 and 500, respectively. Trends in the signal from SPND-D match well between cycle 498 and 500, as well as with the HFIRCON model. Intentional temperature transients during irradiation revealed a significant temperature sensitivity in the SPND signal, with an inverse relationship between temperature and SPND current.

Irradiation testing of the fiber optic sensors elucidated several important findings. First, it was confirmed that Ge-doped SiO_2 optical fibers suffer significant radiation-induced attenuation, with backscattered intensities from SF2 reaching the noise floor of the OBR instrument within days of irradiation. Conversely, F-doped SiO_2 optical fibers showed backscattered intensities that increased relative to pre-irradiation intensities after ~25 d of irradiation in HFIR, at which point this fiber was broken during handling between irradiation cycles. Interestingly, Type II FBGs inscribed in these same fibers suffered >40 dB attenuation and the backscattered intensities in SF5 approached those of SF1, which did not have any inscribed FBGs. Type II FBGs inscribed in fibers with F-doped SiO_2 core and cladding survived irradiation testing over 3 HFIR operating cycles, even at the high neutron flux locations (near the HFIR core centerline). UV gratings inscribed in Ge-doped fibers were particularly susceptible to radiation damage and should not be used in nuclear environments because of their radiation-induced attenuation. Finally, the spectral drift from FBG sensors in SF3/SF4 and SF5 is consistent with the drift observed in the nongrated SF1, indicating that the drift is not an artifact associated with the grating inscription process.

5. ACKNOWLEDGEMENTS

This experiment was sponsored by the Nuclear Science User Facilities Program of the US Department of Energy (DOE) Office of Nuclear Energy. The report was authored by UT-Battelle under contract no. DE-AC05-00OR22725 with DOE. Data analysis was supported by the Advanced Sensors and Instrumentation program of the DOE Office of Nuclear Energy. Neutron irradiation in HFIR was made possible by the DOE Office of Science. The authors acknowledge the help of Shay Chapel, N. Dianne B. Ezell, Kara Godsey, David Bryant, Kory Linton, Maureen Searles, and Adam James in preparing this experiment, as well as Rose Raney and Anthony Birri for reviewing this manuscript.

6. REFERENCES

[1] R.D. Cheverton and T.M. Sims. HFIR Core Nuclear Design. Report ORNL-4621, Oak Ridge National Laboratory, 1971.

[2] Padhraic L. Mulligan, Kurt R. Smith, N. Dianne Bull-Ezell, Daniel C. Sweeney, Kara M. Godsey, Adam J. James, Annabelle G. Le Coq, Joel McDuffee, Jorge Carvajal, and Christian M. Petrie. Wireless Instrumented RB Experiment Preliminary Design and Analysis. Technical Report

ORNL/TM-2020/1879, Oak Ridge National Laboratory (ORNL), Oak Ridge, TN (United States), 2020.

[3] Padhraic L. Mulligan, N. Dianne Ezell, Kurt Smith, Kara Godsey, Dan Sweeney, Christian Petrie, and Jorge Carvajal. In-Core Neutron Flux, Temperature, and Pressure Instrumentation for the WIRE-21 Experiment in the High Flux Isotope Reactor. Technical report, Oak Ridge National Laboratory (ORNL), Oak Ridge, TN (United States), 2021.

[4] Christian Petrie, Daniel C. Sweeney, Padhraic L. Mulligan, Kara Godsey, N. Dianne Ezell, Paul Sirianni, Shawn Stafford, Jeff Arndt, and Jorge Carvajal. WIRE-21 Experiment Irradiation Conditions and In-Situ Data Collection. Technical Report ORNL/TM-2023/2879, Oak Ridge National Laboratory (ORNL), Oak Ridge, TN (United States), 2023.

[5] Padhraic L Mulligan, Kara Godsey, Daniel C. Sweeney, Shay Chapel, N Dianne Ezell, Shawn Stafford, Jeff Arndt, Jorge Carvajal, and Christian Petrie. Preliminary Data and Thermal Modeling of In Situ Wireless Sensor Irradiation in the High Flux Isotope Reactor. Technical report, Oak Ridge National Laboratory (ORNL), Oak Ridge, TN (United States), 2022.

[6] Christian Petrie, Shay Chapel, Padhraic L. Mulligan, David Bryant, Daniel C. Sweeney, Adam James, N. Ezell, Kurt Smith, Kara Godsey, Maureen Searles, et al. Wire-21 Sensor Irradiation Experiment Ready for HFIR Insertion. Technical Report ORNL/TM-2022/2354, Oak Ridge National Laboratory (ORNL), Oak Ridge, TN (United States), 2022.

[7] Mark Froggatt and Jason Moore. High-Spatial-Resolution Distributed Strain Measurement in Optical Fiber with Rayleigh Scatter. *Applied Optics*, 37(10):1735–1740, 1998.

[8] Daniel C. Sweeney, Dennis M. Sweeney, and Christian M. Petrie. Graphical Optimization of Spectral Shift Reconstructions for Optical Backscatter Reflectometry. *Sensors*, 21(18):6154, 2021.

[9] Daniel C. Sweeney, Adrian M. Schrell, and Christian M. Petrie. An Adaptive Reference Scheme to Extend the Functional Range of Optical Backscatter Reflectometry in Extreme Environments. *IEEE Sensors Journal*, 21(1):498–509, 2020.

[10] Daniel C. Sweeney and Christian M. Petrie. Expanding the range of the Resolvable Strain from Distributed Fiber Optic Sensors Using a Local Adaptive Reference Approach. *Optics Letters*, 47(2):269–272, 2022.

[11] Joseph B. Kruskal. On the Shortest Spanning Subtree of a Graph and the Traveling Salesman Problem. *Proceedings of the American Mathematical Society*, 7(1):48–50, 1956.

[12] Andrew Biggerstaff Lewis and Stuart John Russell. Fibre Optic Distributed Sensing, April 17 2018. US Patent 9,945,717.

[13] Christian M. Petrie and Daniel C. Sweeney. Enhanced Backscatter and Unsaturated Blue Wavelength Shifts in F-Doped Fused Silica Optical Fibers Exposed to Extreme Neutron Radiation Damage. *Journal of Non-Crystalline Solids*, 615:122441, 2023.

[14] E.J. Friebele and M.E. Gingerich. Radiation-Induced Optical Absorption Bands in Low Loss Optical Fiber Waveguides. *Journal of Non-Crystalline Solids*, 38-39:245–250, 1980. XIIth International Congress on Glass.

[15] Christian M. Petrie, Anthony Birri, and Thomas E. Blue. High-Dose Temperature-Dependent Neutron Irradiation Effects on the Optical Transmission and Dimensional Stability of Amorphous Fused Silica. *Journal of Non-Crystalline Solids*, 525:119668, 2019.

[16] Mohamed A.S. Zaghloul, Mohan Wang, Sheng Huang, Cyril Hnatovsky, Dan Grobnic, Stephen Mihailov, Ming-Jun Li, David Carpenter, Lin-Wen Hu, Joshua Daw, et al. Radiation Resistant Fiber Bragg Grating in Random Air-Line Fibers for Sensing Applications in Nuclear Reactor Cores. *Optics Express*, 26(9):11775–11786, 2018.

[17] Charles Daily, Scott Mosher, Stephen D. Wilson, and David Chandler. HFIRCON Version 1.0.5 User Guide. Technical Report ORNL/TM-2020/1742, Oak Ridge National Laboratory, 2020.

[18] Scott W. Mosher and Stephen C. Wilson. Algorithmic Improvements to MCNP5 for High-Resolution Fusion Neutronics Analyses. *Fusion Science and Technology*, 74(4):263–276, 2018.

[19] Ian C. Gauld, Georgeta Radulescu, Germina Ilas, Brian D. Murphy, Mark L. Williams, and Dorothea Wiarda. Isotopic Depletion and Decay Methods and Analysis Capabilities in SCALE. *Nuclear Technology*, 174(2):169–195, 2011.

[20] Scott W. Mosher, Aaron M. Bevill, Seth R. Johnson, Ahmad M. Ibrahim, Charles R. Daily, Thomas M. Evans, John C. Wagner, Jeffrey O. Johnson, and Robert E. Grove. ADVANTG—An Automated Variance Reduction Parameter Generator. Technical Report ORNL/TM-2013/416, Oak Ridge National Laboratory, 2013.

[21] David Chandler, Benjamin R. Betzler, Eva E. Davidson, and Germina Ilas. Modeling and Simulation of a High Flux Isotope Reactor Representative Core Model for Updated Performance and Safety Basis Assessments. *Nuclear Engineering and Design*, 366:110752, 2020.

[22] O. Moreira and H. Lescano. Analysis of Vanadium Self Powered Neutron Detector's Signal. *Annals of Nuclear Energy*, 58:90–94, 2013.